2017

Characterization of ice adhesion strength over different surfaces pertinent to aircraft anti-/de-icing

Prashanth Sagar Reddy Beeram
Iowa State University

Characterization of ice adhesion strength over different surfaces pertinent to aircraft anti-/de-icing

by

Prashanth Sagar Reddy Beeram

A thesis submitted to the graduate faculty

in partial fulfillment of the requirements for the degree of

MASTER OF SCIENCE

Major: Aerospace Engineering

Program of Study Committee:
Hui Hu, Co-major Professor
Wei Hong, Co-major Professor
Ashraf Bastawros

The student author, whose presentation of the scholarship herein was approved by the program of study committee, is solely responsible for the content of this thesis. The Graduate College will ensure this thesis is globally accessible and will not permit alterations after a degree is conferred.

Iowa State University

Ames, Iowa

2017

DEDICATION

This thesis is dedicated to my parents for their beloved support.

TABLE OF CONTENTS

LIST OF FIGURES

LIST OF TABLES

NOMENCLATURE

γ_{SL} - solid-liquid interaction energy

γ_{LG} - liquid-gas interaction energy

γ_{SG} - solid-gas interaction energy

Θ_C - young's contact angle

w_A - work of adhesion

τ - adhesion shear stress

f_x - peak shear force

A - contact area

D - diameter of ice sample

T - thickness of ice container

H - height of the ice sample

δ - probe height from the substrate

Θ_a - advancing contact angle

Θ_r - receding contact angle

r - roughness ratio

f - solid-liquid contact area fraction

R_a - average roughness

Y - elastic modulus

υ - poisson's ratio

ACKNOWLEDGEMENTS

I would like to express my sincere thanks to my major advisor Dr. Hui Hu, whose expertise and guidance has supported me during my entire Master's program. Without his generous help, this thesis would not have been possible. It was an honor for me to be part of his research group and will always be grateful for the opportunity to work under him.

My heartily appreciation also goes to my co-advisor, Dr. Wei Hong, for helping me initiate this research and being involved in my thesis committee. I would also like to thank Dr. Ashraf Bastawros for his decision to be my committee member. I am grateful to him for allowing me to conduct surface topography analysis in his research lab. I would like to thank all my committee members for evaluating my research work and giving me insightful comments.

I would like to thank Mr. Andrew Jordan, Ms. Christine Nelson and Mr. James Benson for their help on setting up my experimental facilities. In addition, I would like to thank our former and current graduate program coordinators, Ms. Jackie Kester and Ms. Sara Goplin for providing timely information and assistance regarding the program.

I am especially grateful to our former post-doctoral associate, Dr. Rye Waldman, for his valuable contribution to my research. I also want to thank my research colleagues Dr. Wenwu Zhou, Dr. Haixing Li, Dr. Yang Liu, Mr. Bishoy Dawood, Mr. Pavithra Premarathne, Mr. Linkai Li, Mr. Zhe Ning, Mr. Liqun Ma, Ms. Linyue Gao, Mr. Avinash Saikia, Mr. Pengming Sun for their co-operation and assistance.

Finally, I would like to thank my parents Jayapradha and Lakshmi Narayana Beeram for their support to pursue my graduate education at Iowa State University.

ABSTRACT

Aircraft icing is widely recognized as a significant hazard to aircraft operations in cold weather. Several anti-/de-icing systems have been developed recently for aircraft icing mitigation and protection, which can generally be classified into two categories: active and passive methods. While active methods rely on energy input from an external system for the anti-/de-icing operation, passive methods take advantage of the physical properties of the surfaces to prevent ice formation and accretion. While there is no known passive system that can eliminate ice formation over the protected surfaces, passive anti-/de-icing methods, especially ice phobic surface coatings, have been proved to be very helpful to mitigate the problematic effects of icing for various icing related applications.

In the present study, a comprehensive study was conducted to characterize ice adhesion strength over various surfaces by using a custom-built shear strength tester. The studied surfaces include recently developed functionalized surfaces like Slippery Liquid-Infused Porous Surfaces (SLIPS) and commercially-available surface coatings like Hydrobead®, NeverWet®; polymer-based surfaces such as PMMA and PTFE, and metals like aluminum and stainless-steel. In addition, the static and dynamic contact angles for all the control surfaces were also measured to correlate the measured ice adhesion strength with the surface wettability. Furthermore, surface topography analysis was performed to acquire the 3-D surface profiles along with the averaged surface roughness to examine the effects of surface roughness on ice adhesion strength. Similarly, the ice adhesion strength was also analyzed at different temperatures (i.e., -5^0C, -10^0C, -15^0C and -20^0C) to reveal the temperature effects on the ice adhesion strength over hydrophilic and hydrophobic

surfaces. The influence of the durability of surface coatings on the ice adhesion performance of hydro-/ice-phobic coatings was also investigated experimentally in the present study. In coordinating with the experimental study, a numerical analysis was also performed to explore/optimize experimental design paradigms to minimize the measurement uncertainties.

CHAPTER I
INTRODUCTION

1.1 Aircraft Icing

Aircraft Icing can create significant problems to the overall performance and control of the aircraft. The ice accretion on critical surfaces like aircraft wings usually result in the loss of lift and thrust in addition to the gain in weight and drag [Bragg et.al, 2005]. Moreover, the ice shedding from the aircraft surfaces can also damage the airframe and engine components [Bassey and Simpson 2007]. Other icing effects can also include the loss of radio communications, loss of operation of control surfaces, brakes, and landing gear.

Over the years, there were number of aircraft icing related accidents and incidents that caused several deaths of personnel and extensive damage of property. It was observed that 944 icing related accidents and incidents occurred in US from 1978 to 2005 [Green, 2006]. Further between the years 2006 to 2010, 258 icing related accidents and incidents was revealed from the NTSB and ASRS databases [Appiah-Kubi, 2011]. It also the includes one of the major icing related accident in 2009 where four crew members and 45 passengers onboard the Bombardier Inc. DHC- 8- 402 twin engine aircraft were killed near the Clarence Center, New York.

Around forty percent of the accidents in these investigations were attributed to inflight icing occurring on the wings, fuselage or control surfaces. The inflight ice accretion phenomenon is caused by the impingement of supercooled water droplets in the atmosphere. The weather conditions such as the temperature, water content and droplet

size results in the formation of ice over the aircraft surface. The ice accretion is primarily classified as rime ice and glaze ice based on the ice structure and appearance. The glaze ice is formed when the water droplets deform and/or flow over the surface prior to the freezing process resulting in a hard and transparent appearance [Hansman and Kirby, 1987]. Moreover, when the liquid droplets freeze instantly upon impact develops rime ice which is brittle, opaque and tends to grow in the airstream. It is found that the glaze ice poses more threat to the performance than the rime ice due its runback process that covers more area. An example for glaze and rime ice formation is illustrated in Figure 1.1 from the study of dynamic ice accretion on UAS propellers by Liu and Hu [2015] at Iowa State University.

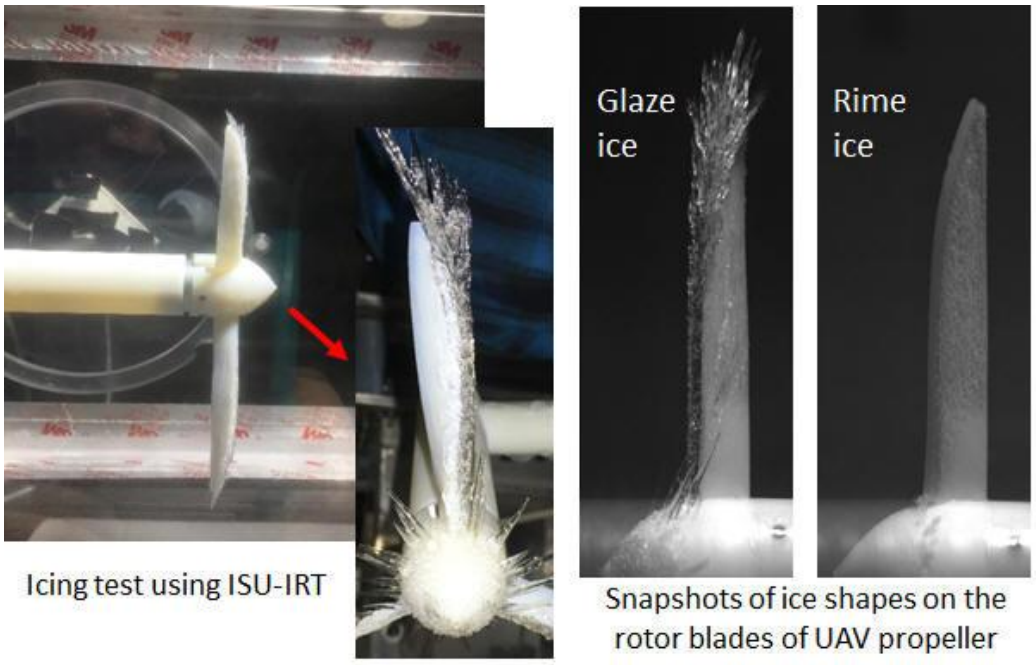

Figure 1.1 Formation of glaze and rime ice on propeller blades [Liu and Hu, 2017]

1.2 Ice Protection Systems (IPS)

To address the potential impacts of aircraft icing, research on developing an efficient ice protection system is highly sought-after. Currently, there are several ice protection systems in use based on specific type of aircraft which can either prevent the ice formation (Anti- Icing) or enhance the removal of ice (De-Icing). The following section gives a description of some of the ice protection systems based on the FAA Advisory Circular 91-74B [2015].

1.2.1 De-Icing Systems

***Pneumatic boots*: -** It comprises of rubber tubes attached to critical aircraft surfaces, such as the leading edges of wings and horizontal and vertical stabilizers. The tubes are made of air filled chambers which may be aligned either chordwise or spanwise. The adhesive bond between the ice and rubber is designed to break by change in the shape of the boots by inflating the rubber tubes. The pneumatic boot system is mostly used in low and medium speed aircrafts with propeller and turbo propeller engines.

***Electro-Impact or Electro-Mechanical*: -** This system uses mechanical force to remove the ice from the aircraft surface using actuators located underneath the skin. The actuators transmit pulses of energy directly to the ice interface and dislodge the ice. Several mechanisms of actuation can be used including ultrasonic, piezoelectric based.

***Electro-thermal*: -** deices a surface by heating the surface to a temperature above freezing to break the bond of accumulated ice. The shattered ice is then carried away by the airflow. The surface is allowed to cool to allow ice to form, and the heat is activated

again to shed the ice, thus repeating the cycle of deicing. The heat generation from continuous operation of conductive element also serves as anti-icing protection.

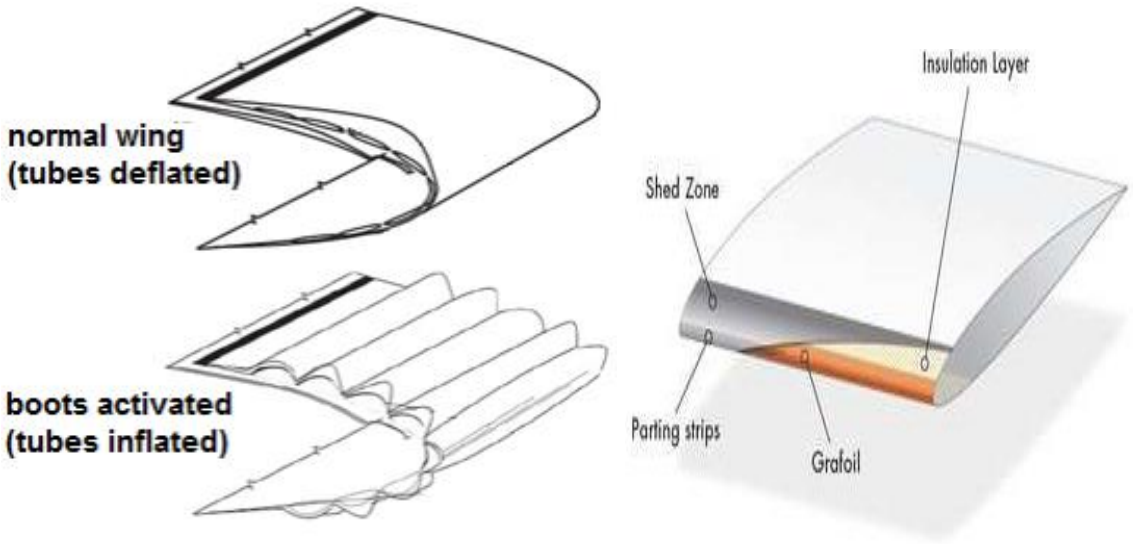

(a) Pneumatic Boots (b) Electro-Thermal

Figure 1.2 Ice protection systems

1.2.2 Anti-Icing Systems

***Bleed air IPS*: -** Bleed air system is used by most turbojet and turboprop aircrafts in which a pressurized hot air from the compressor section of the engine is supplied to ice prone surfaces for eliminating ice formation.

***Evaporative/Running Wet Systems*: -** These systems utilize chemical agent that lowers the freezing point of water found on aircraft surfaces and decreases friction coefficient to prevent ice adherence to the surfaces.

1.3 Challenges of Conventional Ice Protection Systems

The current ice protection systems, in general, require associated components that add complexity and contribute to overall weight of the aircraft. In addition, the operation of electro-thermal and electro-mechanical system result in high cost of electrical power.

Therefore, the energy requirements of the heating and mechanical anti/de-icing devices must be minimized to realize an efficiency benefit from the applications of ice protection techniques. Future generation of aircrafts will require an effective anti-/de-icing solution to extend their operating capabilities, improve safety, and reduce operating costs in cold weather.

1.4 Passive Ice protection systems

In contrast to the conventional ice protection techniques, the passive methods do not have an active control and energy requirement for de-/anti-icing of aircraft surfaces. They use functionalized surfaces which have tendency to repel the liquid water upon contact. Experiments have demonstrated that some superhydrophobic coatings do have icephobic properties [Cao et.al, 2011], that droplets can bounce off cold superhydrophobic surfaces without phase change [Maitra et.al, 2014], and some authors assert that superhydrophobicity directly implies anti-icing functionality [Vorobayev and Guo, 2015].

1.4.1 Superhydrophobic coatings

The superhydrophobicity of the surface depends on the combination of chemical surface energy and the surface texture. The lotus leaf is an example from nature which exhibit superhydrophobic property as a result of its surface with unique protruding features called papillae of varying height [Hensikat et.al, 2011]. The high density of papillae on the lotus leaf reduces the contact area of water by supporting the droplet weight. The reduced contact area with contact angle more than 150^0 causes low adhesion of water helping in water roll off from the surface. Moreover, the papillae are also covered with wax material which reduces the surface free energy of the lotus leaf and enhancing the hydrophobic properties (Figure 1.3).

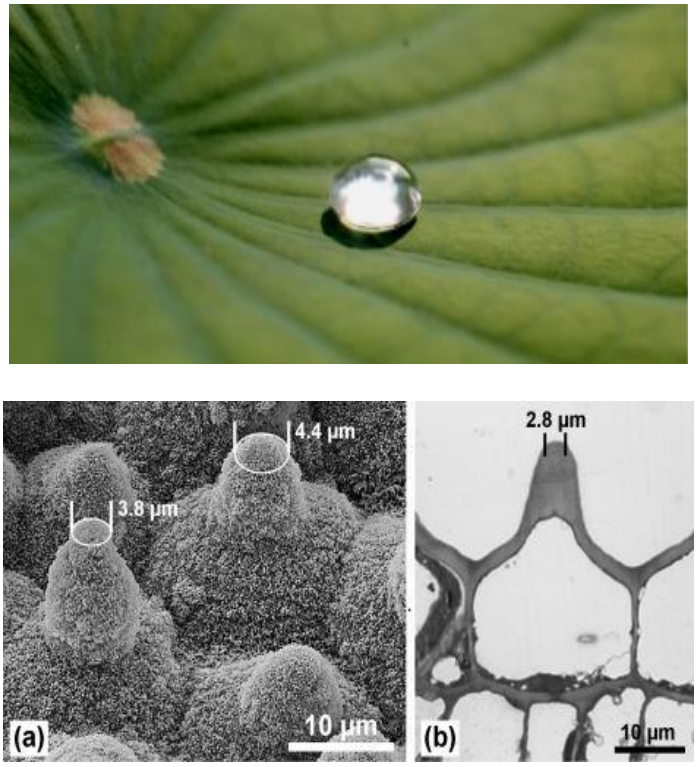

Figure 1.3 SEM image of upper side of lotus leaf with papillae [Ensikat et.al, 2011]

Based on the characteristics of lotus leaf, number of researchers started developing superhydrophobic coatings for other applications. The efforts to incorporate such coating technologies in aircraft ice protection have been going on for long time. An alternate surface coating strategy attempts to reduce the surface adhesion strength by using a lubricating fluid impregnated in the coating matrix [Epstein et.al, 2012, Zhu et.al, 2013]. In these coatings, a lubrication fluid (such as an oil) prevents a strong bond between the ice and the surface. Diffusion replenishes any lubricant lost from the surface (e.g., lubricant is lost during an ice shedding event), making these surfaces robust and self-healing.

Although these coatings proved to reduce the ice formation in static cases, dynamic impingement of the supercooled water droplets at high velocities still found to challenge the effectiveness of this method. Figure 1.4 shows how a superhydrophobic wing surface reduces the area of the wing covered in ice. Here, the aerodynamic stresses from the airflow over the wing surface sweeps away super-cooled water droplets from most of the wing's surface. However, ice still forms at the leading edge in the vicinity of the stagnation line. This highlights one of the major challenges facing water- and ice-phobic coating strategies. These coatings produce low adhesion forces between the water and/or ice and rely on aerodynamic stresses acting tangentially to the surface to remove the accretion. This approach breaks down at the stagnation line because the required shear stress near the stagnation line is very small or completely vanishes. Further exacerbating the problem is that the collection efficiency is a maximum at the stagnation line. This example illustrates how coatings that are effectively ice-phobic at nominal conditions may not perform well under in-flight impact icing conditions.

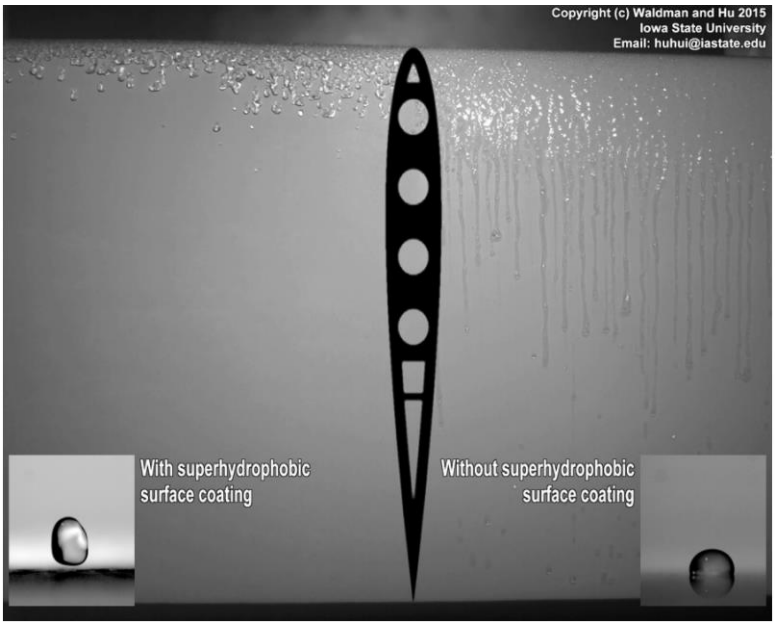

Figure 1.4 Ice accretion on an airfoil with and without a superhydrophobic treatment [Waldman and Hu, 2015]

1.5 Ice Adhesion Mechanisms

Ice adhesion is based on physical and chemical processes that exist between the ice-solid interface. In general, the adhesion forces can be categorized into three different types: chemical adhesion that includes covalent and electrostatic forces; thermodynamic adhesion involving van der Waals forces and hydrogen bonding; mechanical adhesion due to solid surface roughness [Ghalmi et.al, 2009]. In addition, other phenomena such as the presence of the quasi-liquid like layer (QLL) can influence the ice adhesion.

Electro Static Forces: The attraction between the two substrates caused by the transfer of electrons is based on the Coulomb's law and the acceptor-donor interaction [Petrenko and Whitworth, 1999]. It was proposed that adherence of ice is influenced by the electrostatic interaction that exist at the ice-metal interface [Petrenko and Ryzhkin, 1997].

Van der Waals Forces: The Van der Waal forces are regarded as universal, resulting from dipole-dipole interaction. The research by Wilen et al., [1995] concluded that Lifshitz van der Waals (LW) interactions between ice and different materials were not significant compared to the electrostatic interaction.

Hydrogen Bonding: Hydrogen bonding is caused by the distribution of proton (hydrogen atom) between two electronegative atoms such as oxygen, nitrogen or fluorine. These forces are responsible for the cohesion of solid ice from the liquid water [Ghalmi et al., 2009].

Mechanical Bonding: The asperities or pores present on the surface result in the liquid water to penetrate and resulting in mechanical locking or friction after solidification [Kasaai and Farzaneh, 2004]. The mechanical bonds generally occur in micrometer range compared to much smaller length scale of other force mechanisms discussed above. The effect of mechanical bonding can be observed by the surface roughness parameter measured by devices like optical microscopes. Further discussion on the surface roughness parameter will be presented in Chapter 4 of this thesis.

Quasi Liquid Layer (QLL): Several studies have observed a thin liquid layer at the ice-solid interface which influences the ice adhesion. Jellinek [1962] reported that the thickness of the QLL ranges from 100 Å to 1000 Å at -4.5^0 C which corresponds to 30 to 300 water molecules. The QLL thickness was shown to have dependence on the temperature.

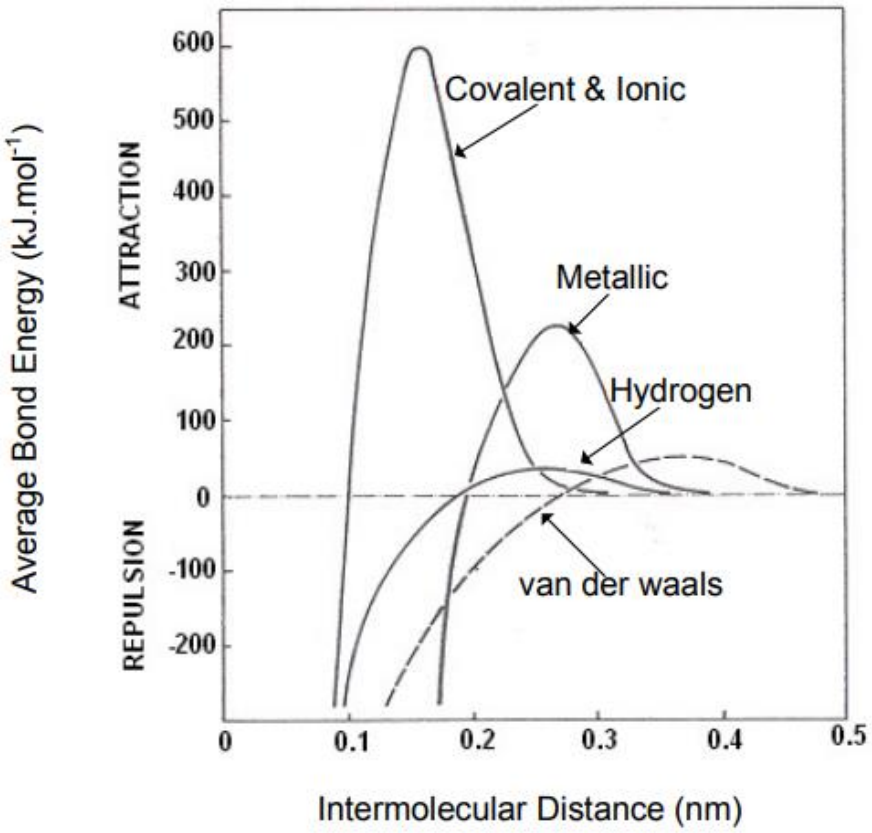

Figure 1.5 Strength and range of the typical intermolecular and interatomic forces [Lee, 1991]

1.6 Ice adhesion Measurement

The theoretical method of estimation of ice adhesion characteristics was based on the calculation of the 'work of adhesion'. The work of adhesion is defined as the free energy required to separate the ice from the solid surface. Figure 1.6 illustrates the water drop on a solid surface in three-phase system of the liquid water in the drop, the solid surface and the surrounding gas. The shape of the droplet is determined by the liquid-solid, liquid-gas, and solid-gas interaction energies denoted by $\gamma_{SL,}$ γ_{LG} and γ_{SG} respectively.

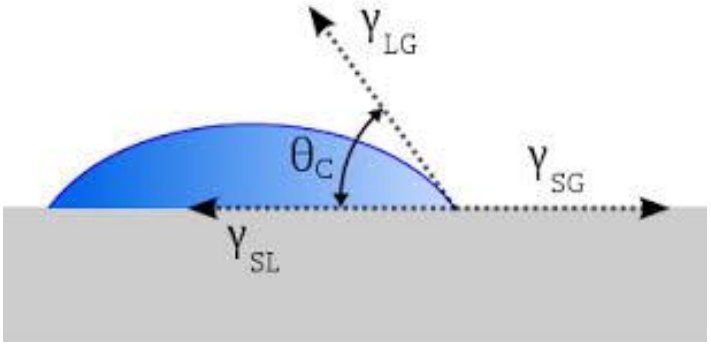

Figure 1.6 Water droplet on a solid surface with contact angle Θ_C

The three-phase equilibrium condition for water droplet is given by Young's equation with contact angle Θ_C which is expressed as

$$\gamma_{LG} \cos \Theta_C = \gamma_{SG} - \gamma_{SL} \quad (1.1)$$

Dupre introduced reversible work of adhesion thermodynamically expressed as

$$w_A = \gamma_{SG} + \gamma_{LG} - \gamma_{SL} \quad (1.2)$$

By combing the two equations, lead to the Young-Dupre equation:

$$w_A = \gamma_{LG} (1 + \cos \Theta_C) \quad (1.3)$$

According to the equation 1.3, the thermodynamic work of adhesion is approximated by the surface tension of liquid and the contact angle of liquid on the solid surface. When the contact angle is zero, the wetting is total and hence show better adhesion. As the contact angle increases, the surface wetting decreases and the material tends to be hydrophobic in nature when Θ_C exceeds 90^0.

Considering the surface energies of water and ice are same and assuming similar interfacial energies at the solid surface, the work of adhesion for water can be approximated to the work of ice adhesion [Makkonen 2012]. In theory, it is expected that the ice removal depends on the contact angle based work of adhesion. However, in reality, macroscale experiments show deviations from the curve shown in Figure 1.7 due to the work spent to overcome material deformation or other factors renders the ice adhesion model complex and difficult to complete.

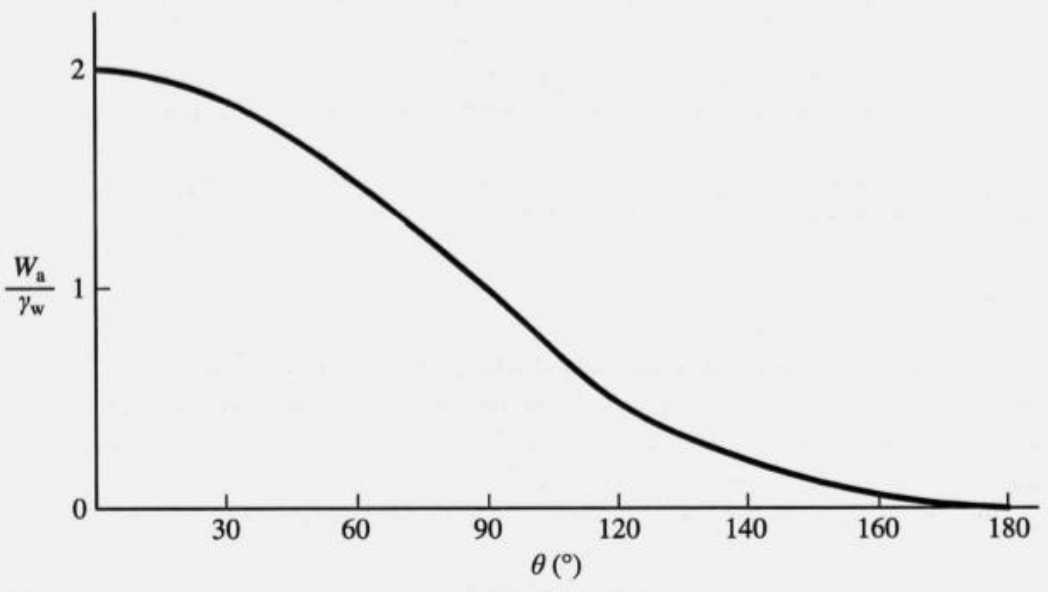

Figure 1.7 Thermodynamic work of ice adhesion scaled by the surface tension of water as a function of water contact angle Θ [Makkonen, 2012]

The theoretical work of adhesion, in general, is not considered as suitable parameter to estimate ice adhesion characteristics. Rather, 'adhesion strength' which is defined as the maximum force required to separate the ice from the substrate is commonly used.

$$\text{Ice Adhesion Strength} = \frac{\text{Maximum force}}{\text{Contact Area}}$$

$$\tau = f_x / A \qquad (1.4)$$

So far, many different techniques to measure the ice adhesion strength have been proposed. The purpose of ice adhesion strength measurement in a broader sense, is to develop an accurate analytical model to predict the ice adhesion over different surfaces. However, it would be extremely difficult in achieving a complete understanding of ice adhesion mechanism because of the number of uncertainties and influential factors involved. The determination of ice adhesion strength would allow better selection of materials for ice protection applications.

1.6.1 Types of Ice Adhesion Strength Measurement

Based on the direction of force applied on ice-solid interface, the adhesion testing can be broadly classified into three modes pure shear test, pure tension test and tests which involve both shear and tensile forces. Figure 1.8 gives the illustrations based on the modes of testing.

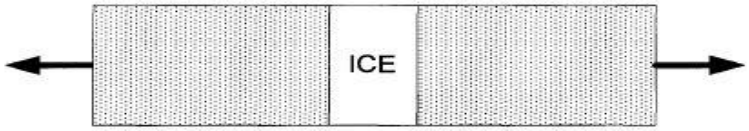

(a) Tension method

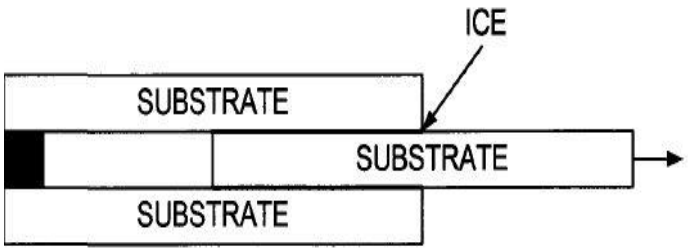

(b) Shear test

Figure 1.8 Testing Modes of Ice Adhesion Strength [Sayward, 1979]

1.6.2 Shear testing

Jellinek [1959] reported that adhesion strength yielded lower values in shear mode when compared to the tension mode. It was explained that the liquid like layer between ice and solid interface results in cohesive failure than adhesion failure during tension mode. Kasaai and Farzaneh [2004] have reported that the shear mode of testing would have more uniform application of load than the tension test.

1.7 Motivation / Objective

Ice adhesion is a complex mechanism which is sensitive to various internal and external factors. So far, concrete testing platforms or procedures to acquire accurate measurement of ice adhesion are unavailable. The existing methods of adhesion testing are used to only estimate the relative ice adhesion characteristics of different surfaces like hydrophobic coatings. In general, the uncertainties due to the experimental method itself poses difficulty in obtaining the true adhesion data. Further, the absence of a comprehensive analytical model for ice adhesion would also make it hard enough to validate the experimental data or even develop a numerical simulation.

The analytical ice adhesion model should address all the common factors of uncertainty including the surface roughness, fracture mechanics, surface chemistry which can be validated by experimental method. This enables to further progress the research on developing ice phobic coatings for aircraft ice protection application.

The Aircraft icing physics and anti-deicing technology laboratory in the department of Aerospace Engineering at ISU is associated with working on the icing physics and modeling, experimental heat transfer and ice accretion processes over different surfaces. The core objective of the research group is to enable us to improve current icing models for more accurate prediction of ice formation and accretion processes as well as to develop more robust anti-/de-icing strategies to ensure safer and more efficient operations of various functional devices in cold weather. The work done for this thesis can be considered to be in conjunction with such broader objective of the research group.

1.8 Thesis Organization

This thesis consists of six chapters in total. An introduction and background to the current study is given in Chapter 1 and the research is summarized with a conclusion in Chapter 6. An appendix is also included to present the additional data and images related to Chapter 3 and 4. A brief summary for each chapter is given below:

Chapter 2 describes the design of the simple/push shear ice adhesion strength testing. The major components of the test rig were divided into three systems and the working mechanism is explained. The standard operating conditions were also given at the end of the chapter.

Chapter 3 presents a quantitative study of ice adhesion strength over different surfaces. The surfaces are divided into hydrophilic, hydrophobic and superhydrophobic based on their contact angles. The surface preparation was explained based on the type of substrate/coating used for the experiment. Further, the ice adhesion characteristics were compared to the contact angle of the surfaces to study the influence of surface wettability on the ice adhesion strength.

Chapter 4 gives the analysis of ice adhesion strength with respect to the extrinsic parameters such as surface roughness and surface temperature.

Chapter 5 introduces a finite element study of the ice adhesion testing model to understand the stress distribution effects at the ice-solid interface. In particular, the estimation of uncertainties involved due to the experimental model was the objective for this numerical simulation.

CHAPTER 2
EXPERIMENT DESIGN AND SETUP

2.1 General Design of the Experiment

The design criteria are based on the concept of pushing the ice sample over the test surface and obtain the ice adhesion strength based on the maximum force applied to break the contact similar to the ice adhesion strength measurement system mentioned by Mueler et al., [2010]. The experimental setup can be essentially categorized into three systems as illustrated in Figure 2.1

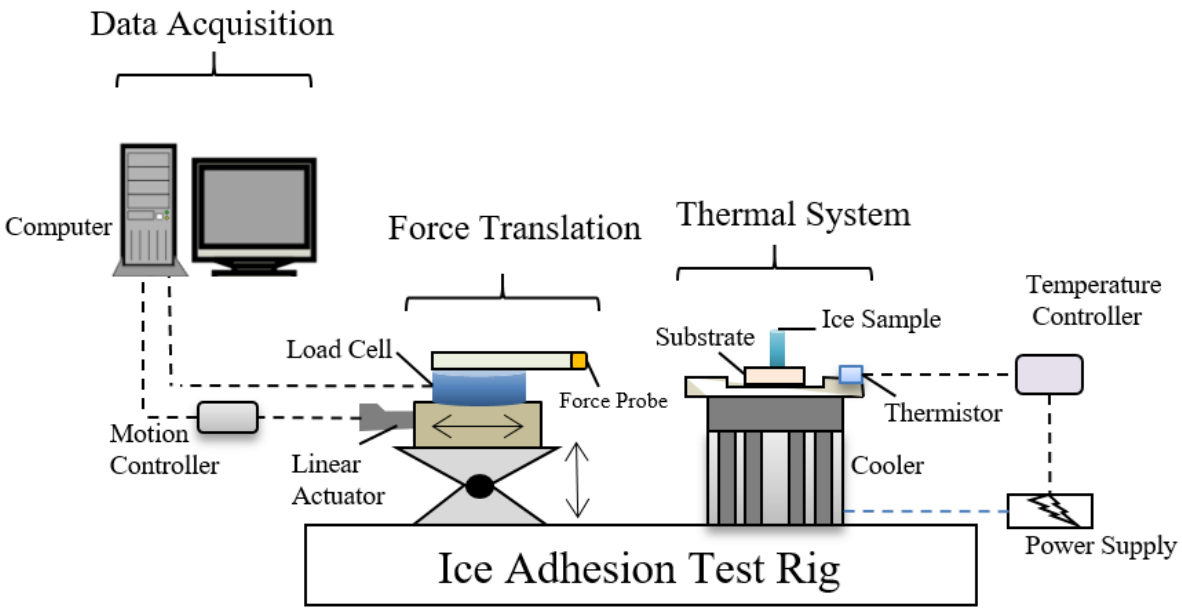

Figure 2.1 Components of ice adhesion test rig

2.2 Description of apparatus

2.2.1 Force Translation

The force on the ice column is applied through an aluminum force probe fixed to a JR3 load cell (model: 30E12A4) which has a nominal force range of 40N range with an extended capacity up to 60 N. The load cell rests on a three-axis linear translational system formed by a lab jack for positioning the height and two linear stages perpendicular to each other for adjusting the force probe in axial and lateral directions. The axial displacement is achieved using a linear actuator (Newport CONEX-LTA-HS)

2.2.2 Thermal System

The experiment consists of a thermoelectric or Peltier cooler from TETech (CP- 061) that can be controlled using an external digital thermal controller (TETech TC-48-20). The temperature ranges for the cooler can be achieved to -20^0 C under ambient room temperature. The thermal controller is also connected to a thermistor sensor (MP-3193) which is fixed to aluminum mounting plate that is attached to the cold side plate of the cooler. The dimension of the cold plate is about 5-inch x 3.15-inch rectangular section with 4 x screw holes to join the mounting plate for the substrate.

In order to minimize the effect of frost/condensation over the test surface and cooler during the freezing process, an environmental chamber was created. Another insulated chamber filled with dry ice was connected to the environmental chamber which helps to flush out the moisture containing air with subliming CO_2 vapors. Figure 2.2 shows the frost formation over the test substrate and cooler regions exposed to surroundings before the installation of the environmental chamber.

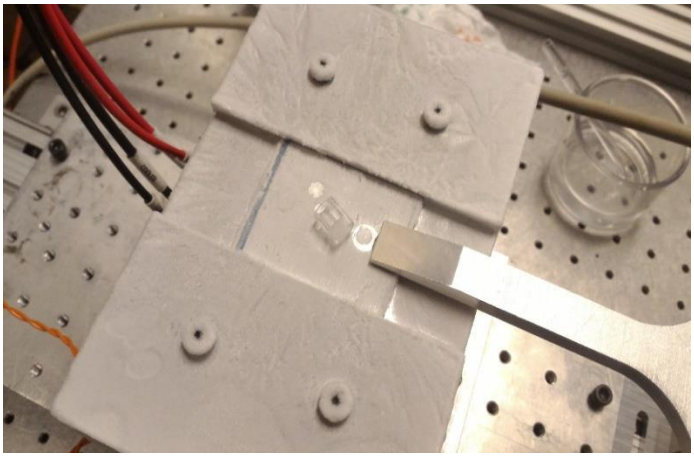

Figure 2.2 Frost formation over the test substrate during freezing process

2.2.3 Ice Sample and Test Substrate Preparation

The test substrates were a 50mm square aluminum plates over which the control surfaces were created. The substrate plate is directly in contact with the cooler with the help of mounting plate machined to fit the substrate inside with only the one surface open for the experiment (Figure 2.3).

The ice samples were created using 3-D printed hollow circular cylinders made of VeroWhite plastic material. The standard thickness for the cylindrical mold was 0.25mm and height was 10mm. The diameter of the ice sample was between 6 mm to 20 mm depending on the test surface and experimental objective.

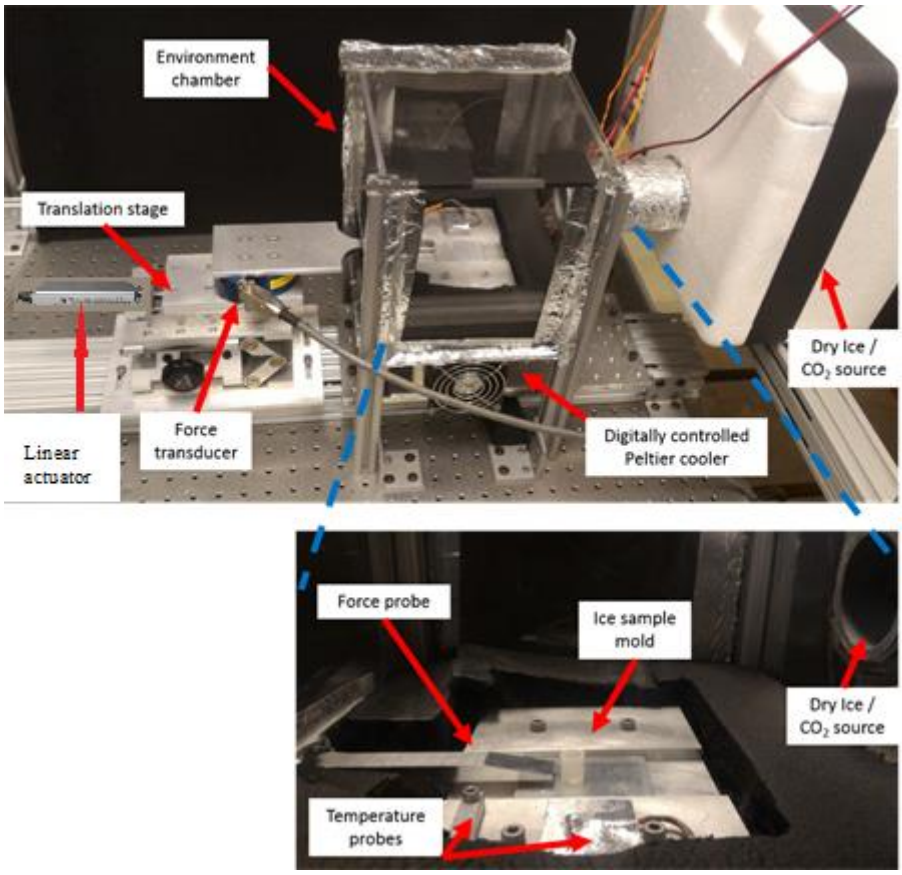

Figure 2.3 Actual configuration of ice adhesion experiment

2.3 Experimental Procedure

The test procedure started with clamping the test plate onto the cooler. Next, the ice mold was placed onto the surface, and a syringe was used to inject deionized water into the mold, ensuring that no air bubbles were trapped underneath. The lid to the environmental chamber was closed, and the chamber was filled with carbon dioxide vapors released from sublimating dry ice. The CO2 displaced the humid air from the test chamber, preventing condensation from forming on the test surface. The Peltier cooler was turned on and set to the test temperature, and allowed to stabilize for 15 minutes, allowing the water sample to freeze and the temperature to remain steady during the test. While the temperature

stabilized, the force probe was aligned with the sample and set at 0.5 mm above the test surface.

A custom MATLAB code sampled the voltage signals from the force transducer at 22000 Samples/s. First a 10 second force tare measurement was recorded prior to bringing the probe into contact with the ice sample. Then forces were recorded while the linear actuator stage was moved at a rate of about 0.5 mm/s, until the sample was sheared of the surface. The MATLAB code applied the transducer's calibration matrix to the voltage signals, and divided by the sample's area to compute the average shear force per adhesion area. The adhesion strength was considered as the maximum force per-area observed before failure. Each test surface was measured multiple times for a reliable measure of the average and standard deviation of the measured adhesion strengths. Table 2.1 gives the experimental parameters for the ice adhesion strength tests mentioned in next chapter.

Table 2.1 Experimental parameters for ice adhesion test

Experimental Parameters	
Cooler Temperature	-8^{0} C
Probe Speed	0.5 mm/s
Freezing Time	30-60 minutes
Sampling Rate	22,000 Hz
No. of trials	10

The experimental results helped to find out the displacement and strain properties of the ice-substrate interface using the force data recorded by the load sensor connected to the probe. In Figure 2.4 (a), the raw data is shown where the ratio of applied force recorded from the load sensor to the ice sample area is plotted for the time elapsed since the initiation of the experiment and until after the ice is broken at the aluminum substrate interface. The maximum value of this ratio or peak stress is considered as the adhesion strength of ice on a surface. From the initial force and time data, we could obtain the displacement result as shown in the Figure 2.4 (b) along with the stress-strain curve in Figure 2.4 (c). The load-displacement curves here depict almost linear relationship which suggests the elastic behavior of ice bonding mechanism. However, a little non-linearity is also visible which could be attributed to the elongation properties of the plastic shell that holds the ice or perhaps it could also be related to the non-linearity of the adhesion mechanism itself.

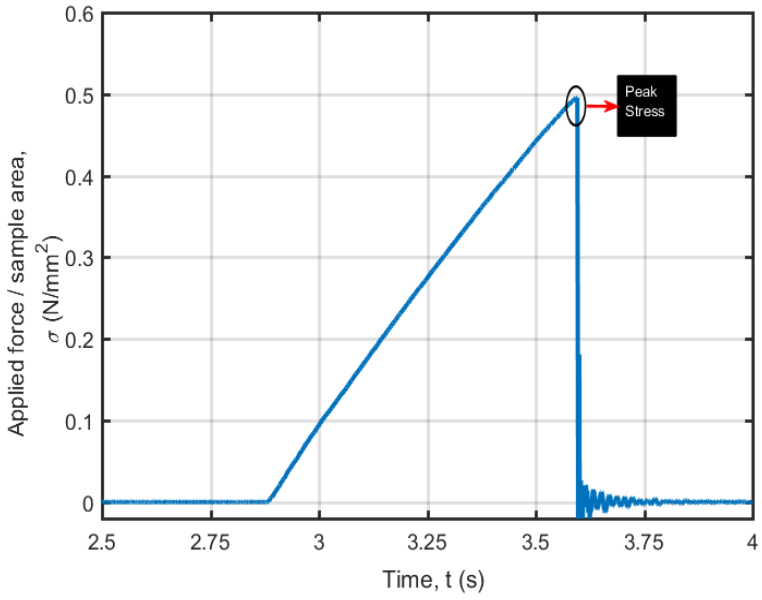

(a) Shear force-per-area vs time

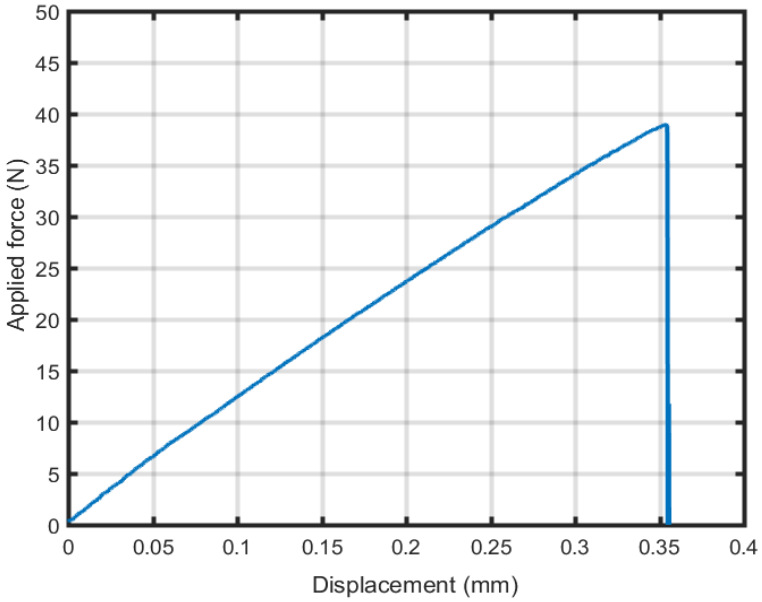

(b) Force vs Displacement

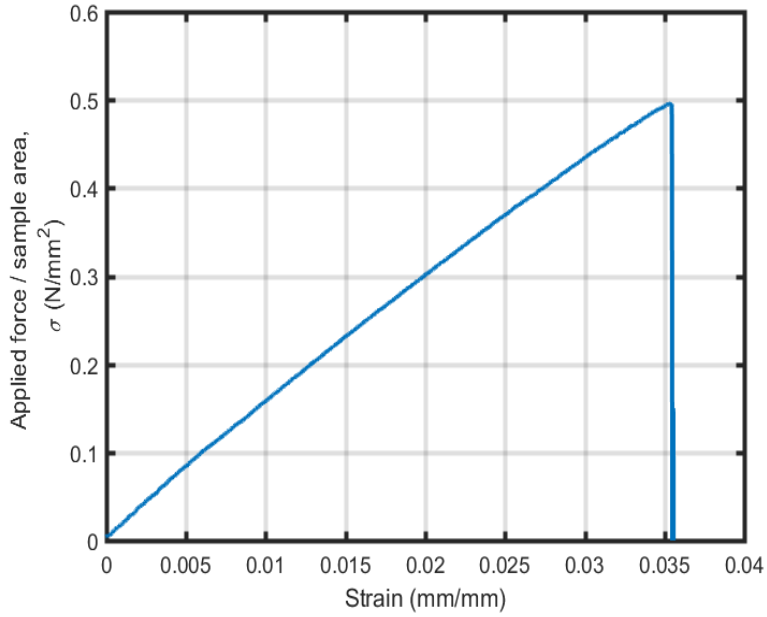

(c) Shear stress vs strain

Figure 2.4 Elastic properties of ice-substrate adhesion mechanism

CHAPTER 3

MEASUREMENT OF ICE ADHESION STRENGTH OVER SURFACES

3.1 Material Selection

The idea of selecting different materials was to identify the behavior of ice adhesion in comparison to the surface characteristics. These surfaces include commercial water repellent coatings like Rust-Oleum NeverWet ®, Hydrobead ® along with recently developed functionalized surface, SLIPS. Metals like Aluminum 6061 and Stainless Steel 316 were also used in addition to some polymers such as PMMA (Acrylic), PTFE (Teflon), PFA and VeroWhite. Rust-Oleum® Enamel protective paint was utilized as the reference to compare the ice adhesion reduction.

3.2 Surface Preparation

Aluminum plates (Al 6061) from McMaster-Carr were cut into 2-inch square section with 0.25-inch thickness were used as a standard base for application of spray coatings or attaching thin polymer films. The bare aluminum and stainless metal surfaces were faced (machining) to remove any rust formation on the testing side of the plates.

The procedure for spray coatings (Hydrobead, NeverWet and Enamel Paint) were based on the manufacturer instructions for each of the specified surface. The aluminum base plate was rinsed with water or isopropanol and allowed to dry thoroughly before the application of any coating. The SLIPS (Slippery Liquid Infused Porous Surface) is that was

prepared by impregnating a thin, porous cloth in oil and stuck to the aluminum substrate. Teflon and PFA sheets/thin films (0.002-in thick) were rigidly adhered without surface wrinkles to the aluminum substrate plate using adhesive and inserted into the mounting plate. Commercially available PMMA/ acrylic plates and 3-D printed VeroWhite plates were prepared with similar dimensions of the aluminum base plate.

3.3 Surface Wettability and Contact Angle Measurement

The wettability characteristic of a surface can be analyzed by measuring the contact angle. As described in Chapter 1, contact angle of water droplet is determined by the three phase equilibrium of liquid, solid and air. The term Θ_C in Young's equation (Eq. 1.1) is usually called the static contact angle applicable for homogenous solids. However, with the real solids, liquids and ambient conditions, Θ_C can vary over time.

The dynamic contact angle (Figure 3.1) is measured during wetting or de-wetting process. Advancing contact angle Θ_a is measured when the water is added in small amount to the initial droplet where the contact angle will be increased while the contact line stays intact. Similarly, the contact angle is reduced when the water is removed in small amount which is attributed to receding contact angle Θ_r. The difference between the advancing and receding contact angles, $\Theta_a - \Theta_r$, is called the contact angle hysteresis.

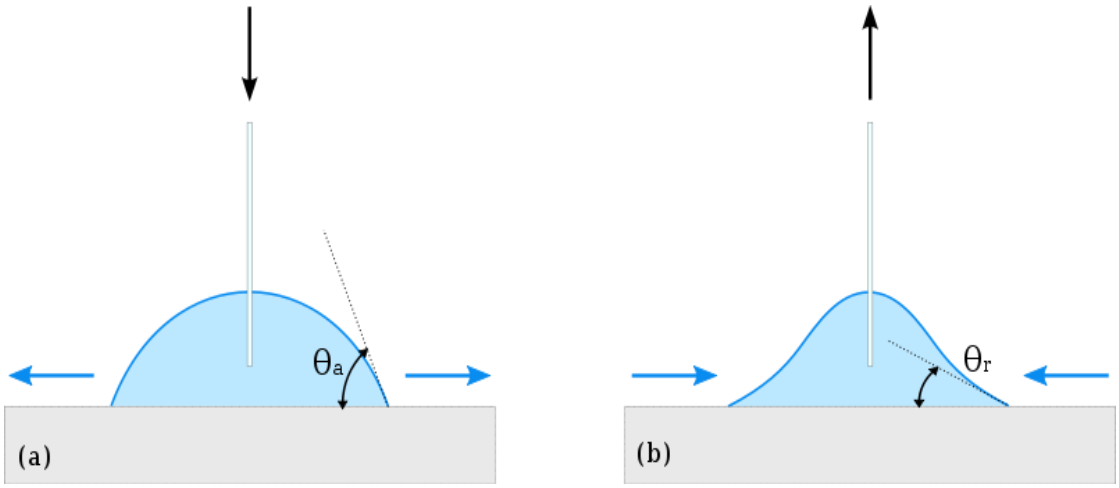

Figure 3.1 Dynamic contact angle (a) Advancing CA (b) Receding CA

Currently, there are several techniques to measure the contact angles. For the current study, Sessile drop technique is utilized in which a high-resolution camera is used to capture the liquid-solid interface and the image is analyzed more often by the imaging software. This technique is applicable for obtaining both static and dynamic contact angles.

3.3.1 Experimental Setup

To characterize the wettability of the test surfaces used in the ice adhesion experiment, the static and dynamic contact angles were experimentally measured. The experimental configuration is depicted in Figure 3.2. A high-speed camera (PCO Tech, Dimax) using 105 mm macro lens (Nikon, 105mm Nikkor 2.8D) was positioned with a view from the side of substrate mounted on vertical lab jack. A syringe is used to pump deionized water through a needle mounted above the substrate, forming a drop that could be expanded and contracted, thereby creating advancing and receding contact line. A 20W led lamp (Dot

Line RPS Studio, RS-5410) illuminating a piece of frosted glass provided back-illumination to provide high-contrast images.

Each substrate was tested by forcing water through the needle using the syringe, thereby creating an expanding droplet with an advancing contact line. Then, the syringe was used to pull the water back into the needle, causing the droplet to shrink and the contact line to recede. The images recorded with the high-speed camera were analyzed using the open source ImageJ software with additional DropSnake plugin for enhanced contact angle measurement. The DropSnake method is based on detecting the global drop contour using B-spline snakes or active contours as depicted in Figure 3.3.

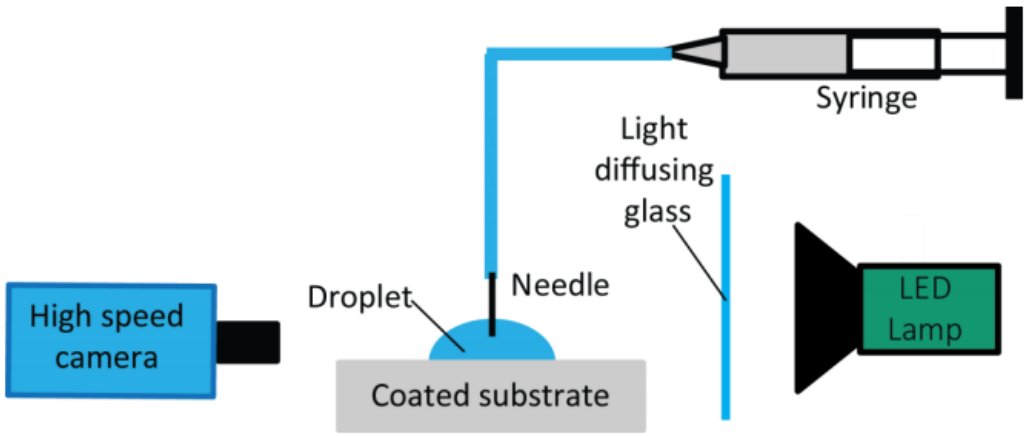

Figure 3.2 Setup for the contact angle measurement

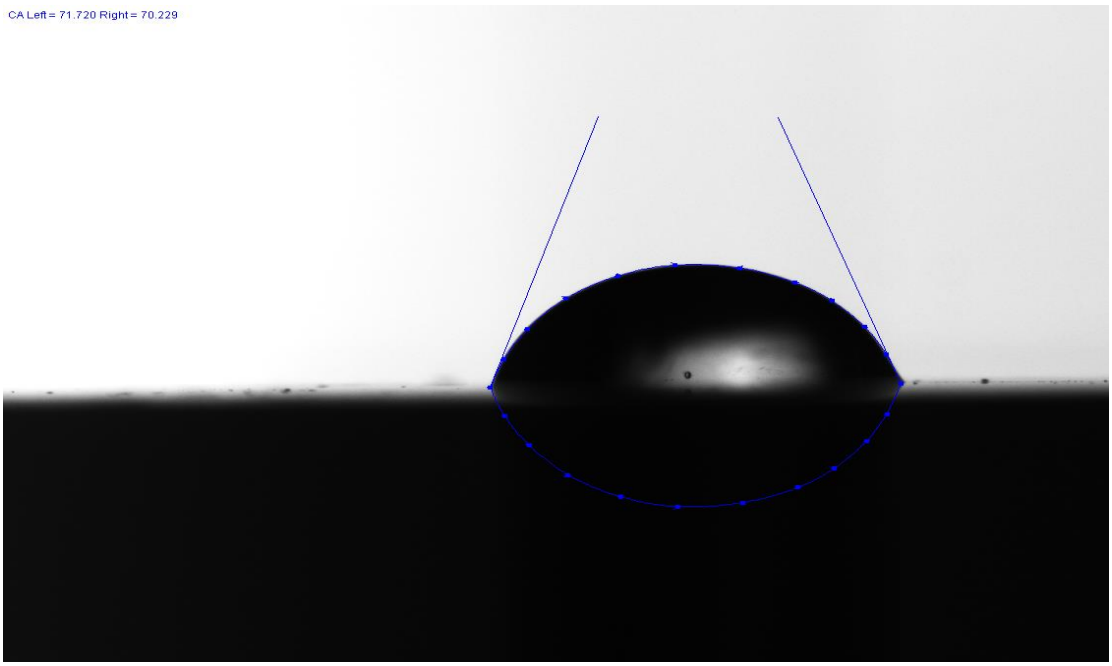

Figure 3.3 Droplet shape analysis for contact angle

3.3.2 Contact Angle Results

The contact angles for 10 different material surfaces were tested to compare their surface wettability. A summary of the measured contact angles is presented in Table 3.1 along with their corresponding water repelling characteristics. Based on the measured contact angles, the surfaces can be divided into three categories namely hydrophilic (CA < 90^0), hydrophobic (CA > 90^0) and superhydrophobic (CA > 150^0).

The enamel surface shows significant contact angle hysteresis when compared to other surfaces with the advancing contact angle and receding contact angle around 104^0 and 20^0 respectively. On the other hand, SLIPS, NeverWet and Hydrobead surfaces exhibited contact angle hysteresis less than 20^0. Interestingly, the static and dynamic

contact angles of SLIPS surfaces are in the hydrophobic range instead of superhydrophobic as seen in the case of Hydrobead and NeverWet coatings.

Table 3.1 Summary of contact angle measurements

Surface	ACA (^{0})	RCA (^{0})	Hysteresis (^{0})	CA Static (^{0})	Wetting Property
Enamel	104	20	84	65	Hydrophilic
Aluminum	71	21	47	68	Hydrophilic
Stainless Steel	86	24	62	75	Hydrophilic
PMMA	82	61	21	73	Hydrophilic
PTFE	98	41	57	95	Hydrophobic
PFA	104	50	54	101	Hydrophobic
VeroWhite	71	20	51	39	Hydrophilic
SLIPS	105	94	11	105	Hydrophobic
Hydrobead	160	148	12	159	Superhydrophobic
NeverWet	155	136	19	153	Superhydrophobic

(a) Advancing CA measurement of Enamel

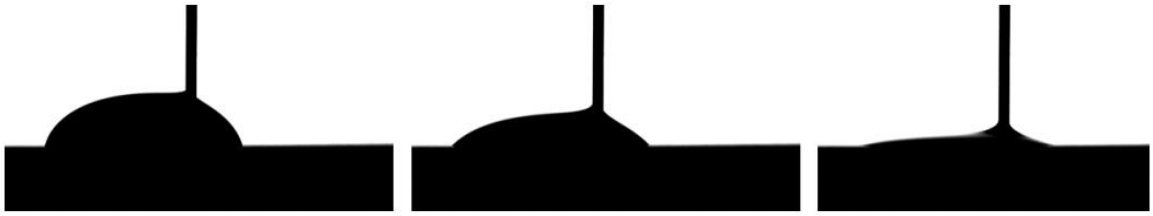

(b) Receding CA measurement of Enamel

(c) Advancing, Receding and Static CA of NeverWet

Figure 3.4 Comparison of dynamic and static contact angles of surfaces with different hydrophobicity

3.4 Ice Adhesion Strength Results

The ice adhesion strengths for the 10 surfaces is presented in the Table 3.2 along with the distribution box plot illustrated in the Figure 3.5. It was observed that Enamel paint exhibited the adhesion shear stress around 1.4 MPa which was also the highest value among the measured surfaces. Since the enamel coating was a reference, the adhesion reduction factor was set to be 1. The hydrophilic metal surfaces like Aluminum and

Stainless Steel were among the surfaces with lowest adhesion reduction factors around 2.5. Moreover, the polymer surfaces excluding PFA such as PMMA, PTFE and VeroWhite showed adhesion reduction factors which were comparatively higher than the metal surfaces. Interestingly, the NeverWet and Hydrobead commercial water repellant coatings were observed to have ice adhesion strength similar to the polymer surfaces. However, only SLIPS can be attributed to exhibit ice phobic properties with the least shear stress of 0.06 MPa recorded.

Table 3.2 Summary of ice adhesion strength results

S.No	Surface	Average Adhesion Strength (MPa)	Std. Deviation (MPa)	Reduction Factor
1	Enamel	1.40	0.13	1.0
2	Aluminum 6061	0.52	0.09	2.5
3	Stainless Steel 316	0.56	0.13	2.5
4	PMMA	0.33	0.05	4.2
5	PTFE	0.42	0.06	3.4
6	PFA	0.57	0.05	2.4
7	VeroWhite	0.39	0.10	3.6
8	SLIPS	0.06	0.01	23.3
9	Hydrobead	0.40	0.09	3.5
10	NeverWet	0.51	0.04	2.7

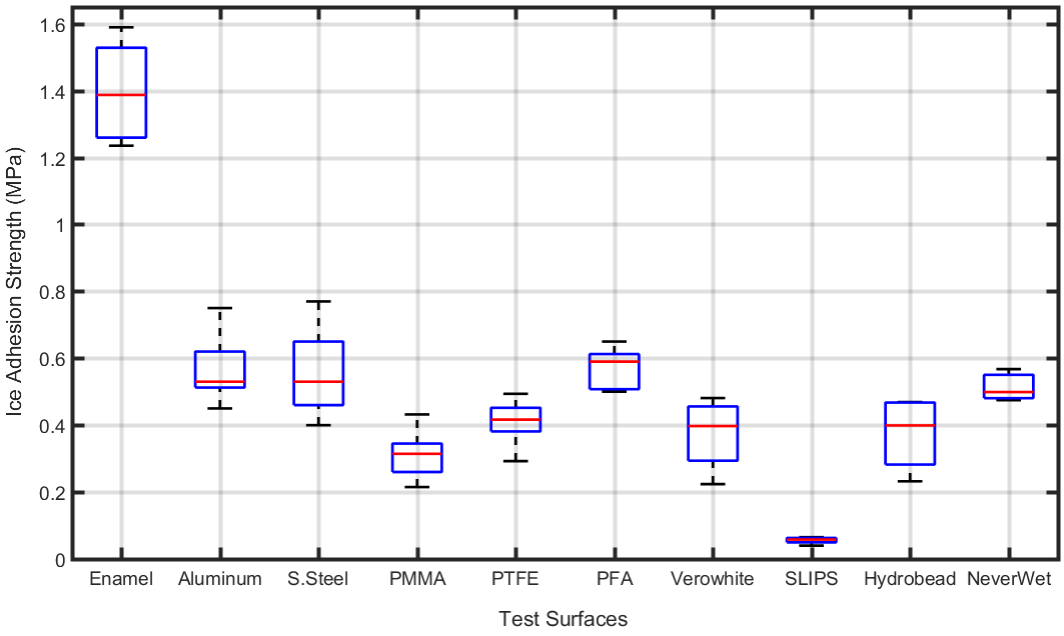

Figure 3.5 Box distribution plot for the ice adhesion strength of surfaces

Further analysis can be made by comparing the ice adhesion strengths of these surface their wetting properties. Figure 3.6 gives the graphic trends showing the static contact angles of the surfaces plotted with the shear stress recorded. Although, the overall trend line in the Figure 3.6 shows a little decrease in shear stress, the inconsistencies in data can be seen in the relation between static contact angle and the ice adhesion strength. In addition, the relation can also be explained by comparing the contact angle hysteresis derived from the dynamic contact angles of the surfaces with the ice adhesion strength. In the Figure 3.7, the overall trend shows that ice adhesion strength increases with the increase in contact angle hysteresis. Similar relationship between CA hysteresis and shear stress was reported by Kulinich and Farzaneh [2009] using aluminum and superhydrophobic polymer surfaces.

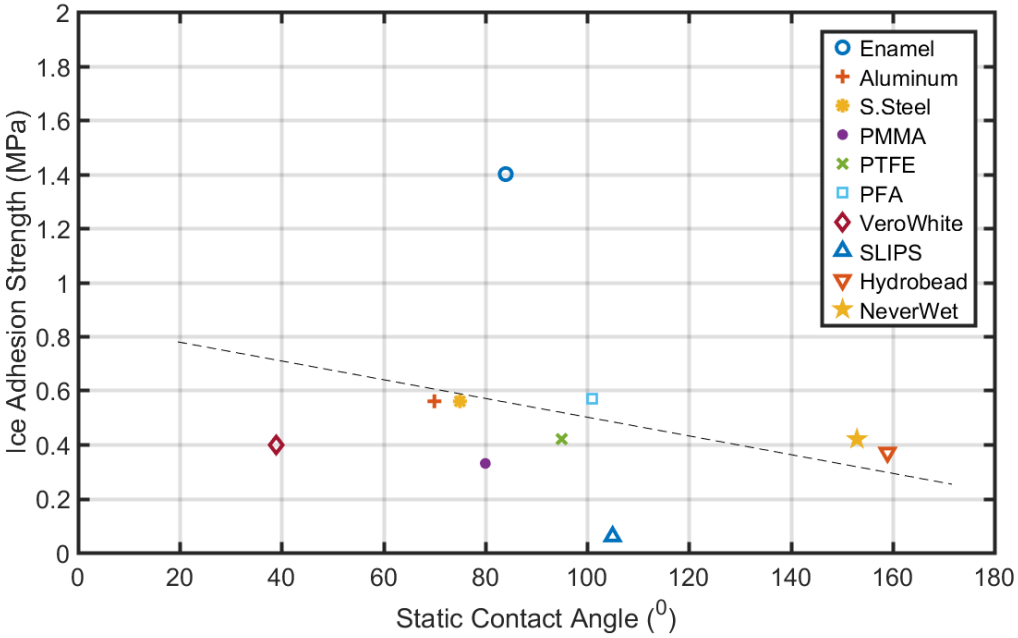

Figure 3.6 Comparison of static contact angle and ice adhesion strength

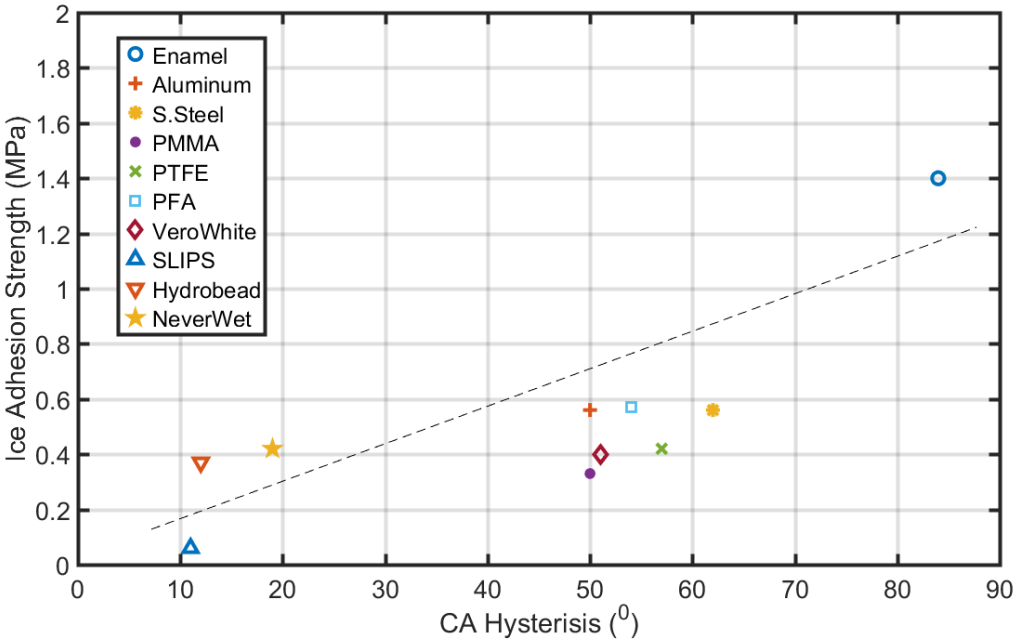

Figure 3.7 Comparison of contact angle hysteresis and ice adhesion strength

CHAPTER 4

CORRELATION STUDY OF SURFACE PARAMETERS

4.1 Effects of Surface Roughness on Adhesion

Surface Roughness or roughness is quantified by the deviations in the normal direction of surface. The magnitude of roughness can be seen in both microscopic and macroscopic levels. Roughness effects the ice adhesion in many ways. The mechanical friction caused by the interlocking and sliding of the surface asperities of ice and surface adds to the force required to break the ice off the surface. Indeed, previous research also showed that the ice adhesion failure can be initiated by the crack propagation resulting from the stress concentration in ice due to the roughness [Hassan 2010, Boluk 1996]. In addition, wettability of liquid is influenced by surface roughness which determines the overall contact area of ice with the substrate.

The Young's Equation as described in Eq.1.1 assumes a homogenous surface without the consideration of surface roughness. Wenzel proposed a theory based on the heterogeneous rough surface. This theory assumes that the surface roughness enhances contact area of solid-liquid interface. The Young's equation is modified using apparent contact angle, Θ^* which is based on the product of the roughness ratio, r and ideal contact angle Θ_C as given in Eq.4.1 [Marmur,2003].

$$\text{Cos } \Theta^* = \text{r Cos } \Theta_C \qquad (4.1)$$

Wenzel's model cannot explain the heterogeneous surface when the liquid-solid contact is incomplete with air trapped between the roughness features as described in Figure 4.1. Cassie and Baxter addressed this limitation with another model which describes the apparent contact angle for heterogeneous surface. The Cassie-Baxter equation is given in Eq.4.2 where f is the fraction of solid surface area wet by the liquid. If f = 1, then the Cassie-Baxter equation would be similar to Wenzel equation.

$$\text{Cos } \Theta^{*} = \text{r. f. Cos } \Theta_c + \text{f -1} \qquad (4.2)$$

The application of Wenzel model and Cassie-Baxter model in practice is based on the contact angle range. When the contact angle is in the range $0^0 < \Theta_c < 90^0$, Wenzel theory is used whereas the Cassie-Baxter equation is used for hydrophobic surfaces with contact angles greater than 90^0.

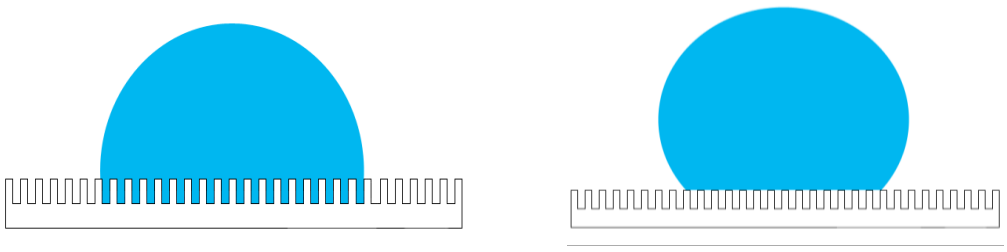

(a) (b)

Figure 4.1 Wetting states of liquid, (a) Wenzel state (b) Cassie-Baxter state

In this study, the effects of surface roughness on ice adhesion were studied based on the results of ice adhesion strength for different surfaces compared with their respective surface roughness.

The bare aluminum substrates are hand polished with sandpaper grits ranging from 220 to 2000 and further with polishing compound to achieve mirror like finish. The procedure for polishing surfaces was based on ASTM standards (E3-11) for metallographic surface preparation. In addition, NeverWet coating was applied with the varied number of coats used to create three different roughness.

4.2 Surface Topography Analysis

The contact angle which is mentioned in the wetting models for practical surfaces depends on the length scales of roughness. Surfaces with hierarchical micro-structures can also influence the hydrophobicity of a surface as described by the Lotus Effect in section 1.5. Since, the roughness plays an important role in the ice adhesion process, measurement of surface through a 3-D surface topography analysis is required to estimate the influence of surface characteristics on ice adhesion strength.

In general, the roughness measurement is commonly described by the parameter R_a (Eq. 4.3) which is the mean roughness calculated from the arithmetic average of the absolute values of the roughness profile that composes peaks and troughs (Figure 4.2)

$$R_a = \frac{1}{n}\sum_{i=1}^{n} |Z_i| \tag{4.3}$$

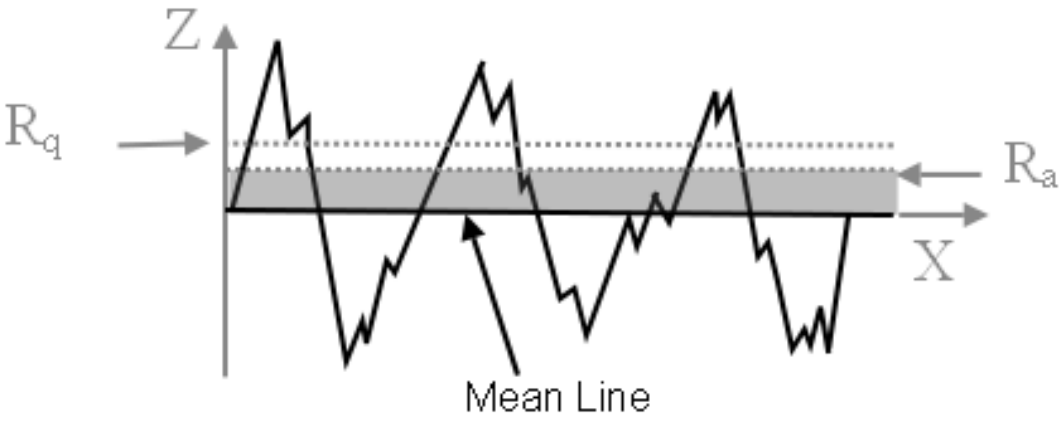

Figure 4.2 Roughness approximation parameters

For the current study, the 3-D surface topography measurement was performed using Zygo NewView optical profilometer. The surface profile was captured using a magnification of 50X and with a field of view around 0.22 x 0.22 mm. The roughness resolution for the profilometer is set to 0.22 ㎜. The summary of the mean roughness for the surfaces is given in Table 4.1 and the surface profiles were shown in Figure 4.3.

The topography analysis shows that polishing bare aluminum with sandpaper grits progressively reduces the surface roughness from 0.6 ㎜ to 0.03 ㎜. Also, the NeverWet spray coating showed higher roughness with the increasing layers of coats. The enamel paint, VeroWhite polymer and SLIPS were observed to have more than 1 ㎜ average roughness.

Table 4.1 Summary of surface roughness (Ra) Measurements

Test Surface	Roughness, Ra (um)
Enamel	1.5
Bare Aluminum	0.6
Al,1000 grit	0.25
Al, mirror-polish	0.03
Stainless Steel	0.19
PFA	0.07
VeroWhite	1.5
SLIPS	1.14
NeverWet, 1	0.3
NeverWet, 2	1.3
NeverWet, 3	3.8
Hydrobead	0.7

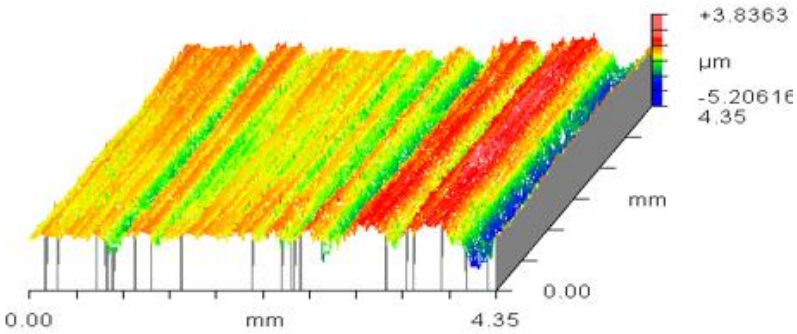

(a) Bare Aluminum

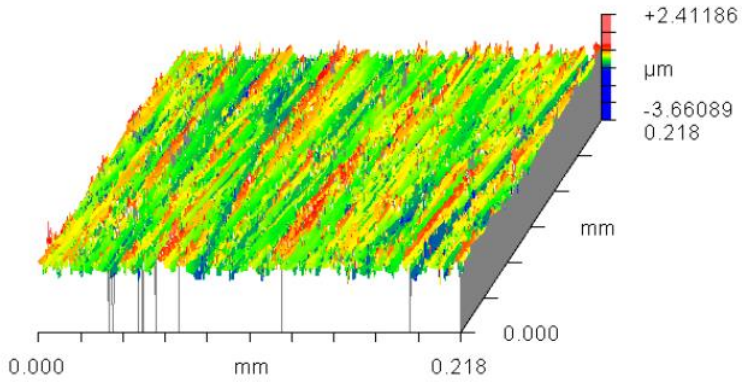

(b) Aluminum, 1000 Grit

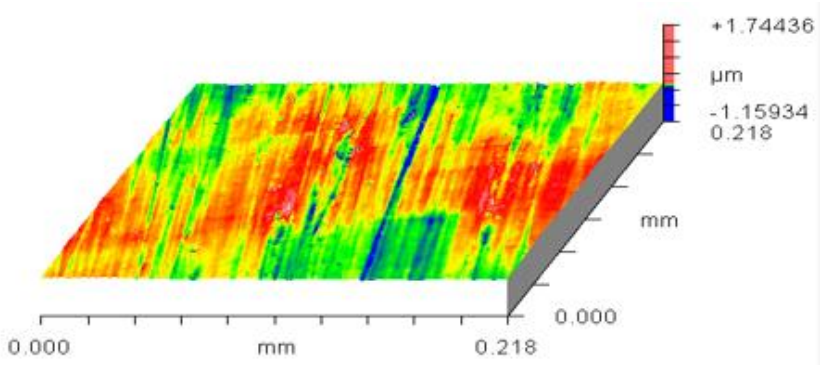

(c) Aluminum, mirror finish

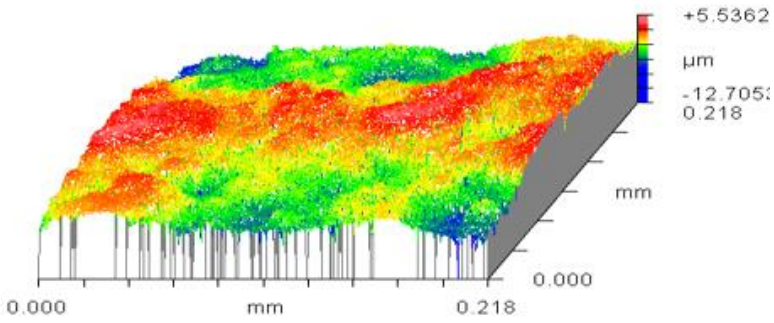

(d) Enamel

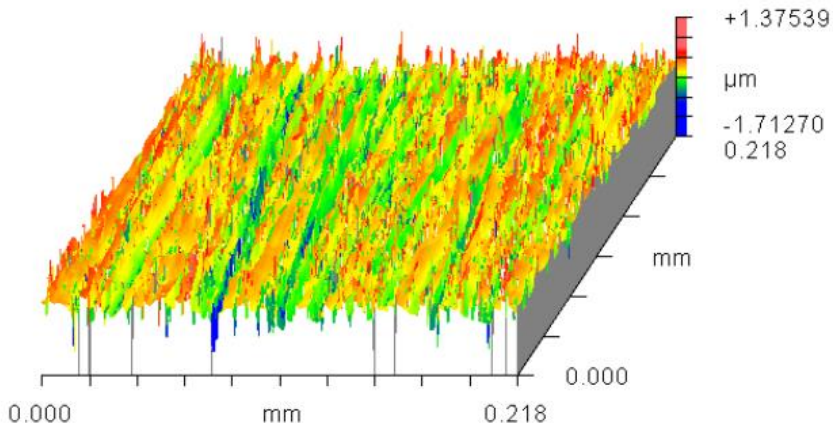

(e) Stainless Steel

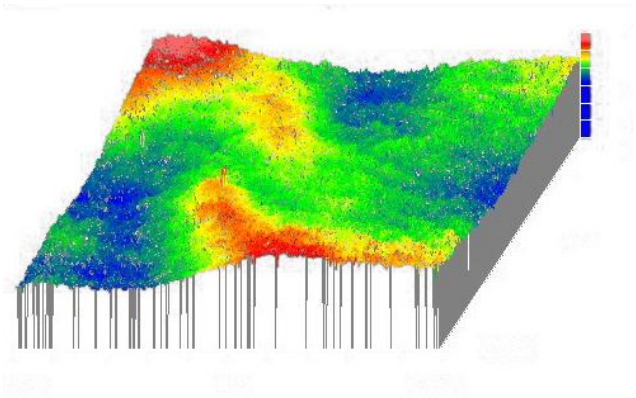

(f) SLIPS

Figure 4.3 Surface Topography Images with 3-D Contour

The influence of surface roughness on the ice adhesion strength can be observed from the Figure 4.4. As described previous section, different roughness profiles were created for Aluminum and NeverWet surfaces. It is observed that, for aluminum surface, the adhesion strength increases with the surface roughness amost linearly. However the NeverWet superhydrophobic surface depicts a contrary trend where its adhesion strenth reduces with increasing roughness.

Evidently, influence of roughness on the ice adhesion depends on the wetting properties. In Figure 4.5, the adhesion strength for 8 surfaces as listed in Table 3.1, is plotted aginst their respective surface roughness. These surfaces were divided into two groups based on their contact angles. The hydrophilic surfaces ($CA<90^0$) marked in blue and the hydro/super-hydrophobic surfaces ($CA>90^0$) are marked in red for comparison. From the figure, it can be noted that the relationship between surface roughness and their corresponding shear stress are not consistent enough to establish a strong linear relationship. However, the comparison between hydrophobic/superhydrophobic and hydrophilic surfaces as a function of surface roughess can be viewed qualitatively in Figure 4.5.

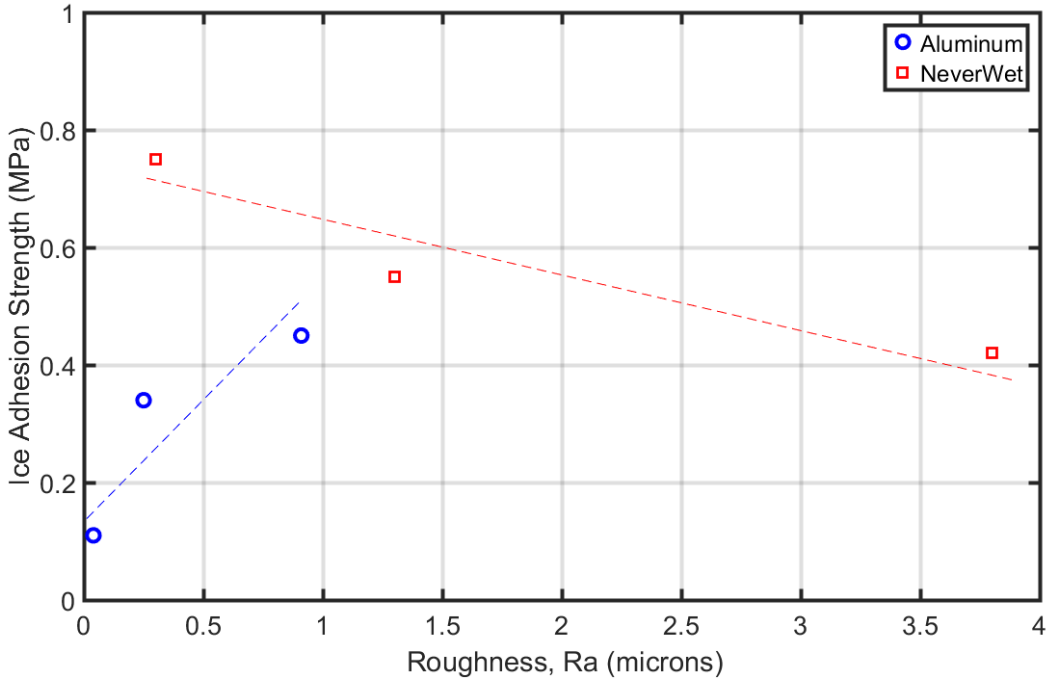

Figure 4.4 Surface roughness vs ice adhesion strength

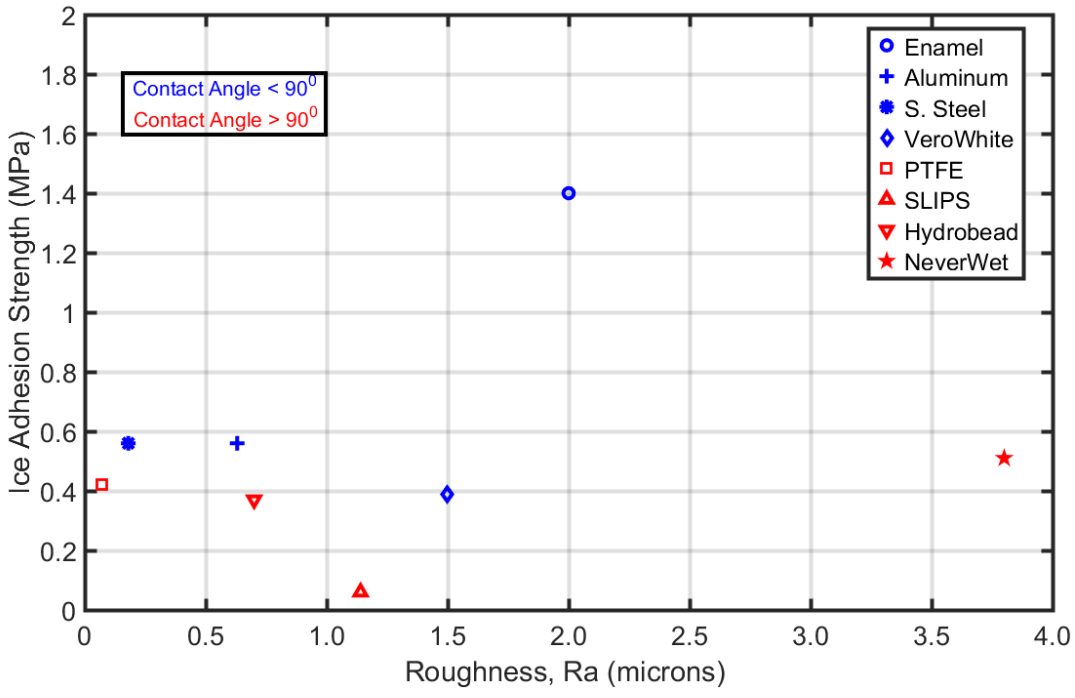

Figure 4.5 Surface roughness vs ice adhesion strength based on hydrophobicity

4.4 Effect of Temperature on Ice Adhesion

Temperature can influence the ice adhesion process through several mechanisms. The wetting characteristics of water and surface could vary at low temperatures due to change in surface tension of water [Heydari, 2016] which induce wetting transitions from a hydrophobic to hydrophilic regime. In addtion, the mechanical properties related to elasticity of solid substrates is directly influenced by the temperature (for example, expansion and contraction in solids with temperature change. Moreover, ice behavior aslo change with temperature, ductile at higher sub-zero temperatures to brittle at much lower temperatures [Jellinek,1959]. Makkonen [2012] reported the stress effects induced by the different thermal contraption of ice and solid surface on cooling. Also, as mentioned in section 1.4 in Chapter 1, the liquid like layer near the ice-solid interface with different properties from water and ice was proposed to be dependent on temperature.

In this study, two superhydrophobic and two hydrophilic surfaces were considered to observe the effect the temperature on ice adhesion strength. The preparation of surfaces was similar to the description in Chapter 3. The temperature of the cooler in this test was set to range from -5 ^{0}C to -20 ^{0}C.

The effect of temperature on ice adhesion strength for these surfaces can be seen from Figure 4.6. The study shows that the ice adhesion strength increase by lowering surface temperature at different gradients. The ice adhesion strength of aluminum, hydrobead and verowhite at -5 ^{0}C are around 0.2-0.3 MPa whereas for the NeverWet, it is 0.61 MPa. The VeroWhite polymer shows a sharp increase in shear stress with lower temperature compared to other surfaces. On the contrary, NeverWet surface shows little dependence on

temperature with a marginal increase from -5 ^{0}C to -20 ^{0}C. Aluminum shows fairly linear change in ice adhesion until -15 ^{0}C and increases further with a lower gradient. Similar trend can be viewed in case of Hydrobead surface where the shear stress increases from 0.19 MPa to 0.51 MPa between -5 ^{0}C and -20 ^{0}C. However, a little downward trend can be observed for SLIPS with adhesion strength below 60 KPa for all the surface temperatures tested indicating better performance at lower temperatures compared to other surfaces.

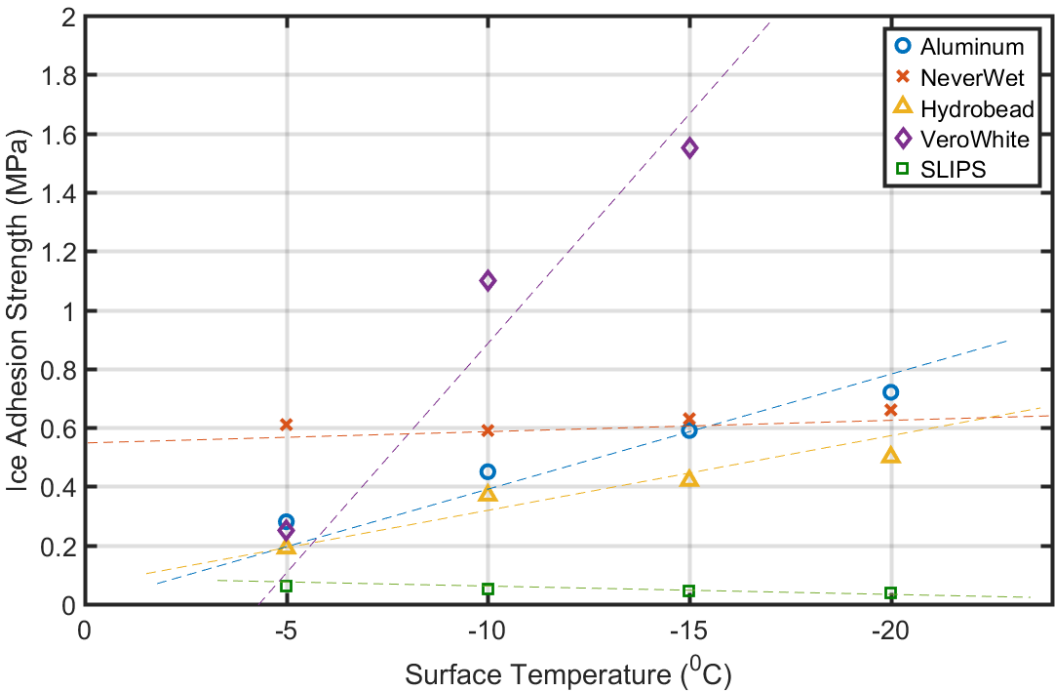

Figure 4.6 Surface temperature vs ice adhesion strength

CHAPTER 5

NUMERICAL ANALYSIS OF ICE ADHESION EXPERIMENT

5.1 Stress Distribution in Ice Adhesion Measurement

The standard methods of calculating ice adhesion strength assume a homogenous stress distribution in which the ice adhesion breaking force is considered as a cumulative parameter for the ice-solid contact area. However, the accuracy of the ice adhesion strength measurement is influenced by the uncertainty of stress concentration in local regions within the ice-solid interface. These local stresses are usually different and appear to be higher than the total stress measured. The adhesion reduction factor as discussed in Chapter 3 can be viewed as a better parameter for comparing the ice adhesion characteristics of different surfaces. However, developing a physical model that can predict the ice mitigation requires accurate measurement of ice adhesion strength that also encompasses the critical stress values existing in the testing model.

Previous studies using finite element numerical analysis by Makkonen [2012] and Schulz [2015] showed the presence of uneven stress distribution in ice-solid interface while using shear strength tests. The numerical analysis has shown the presence both normal and shear stresses as opposed to only shear stress in ideal case. The combination of both stresses resulting in non-uniform load which cannot be resisted by the ice sample causes the crack initiation at high stress regions in the ice-solid interface resulting in poor adhesion strength measurement.

5.2 Model for the Numerical Analysis

A finite element model of the adhesion strength experiment is used to quantify the stress distribution at the ice-substrate interface. A linear statics model was built and solved using ANSYS. The model geometry was defined based on the geometry illustrated in Figure 5.1. The problem size was reduced by a factor of two by using the problem symmetry transverse to the loading direction. Figure 4 gives the schematic for the geometric model.

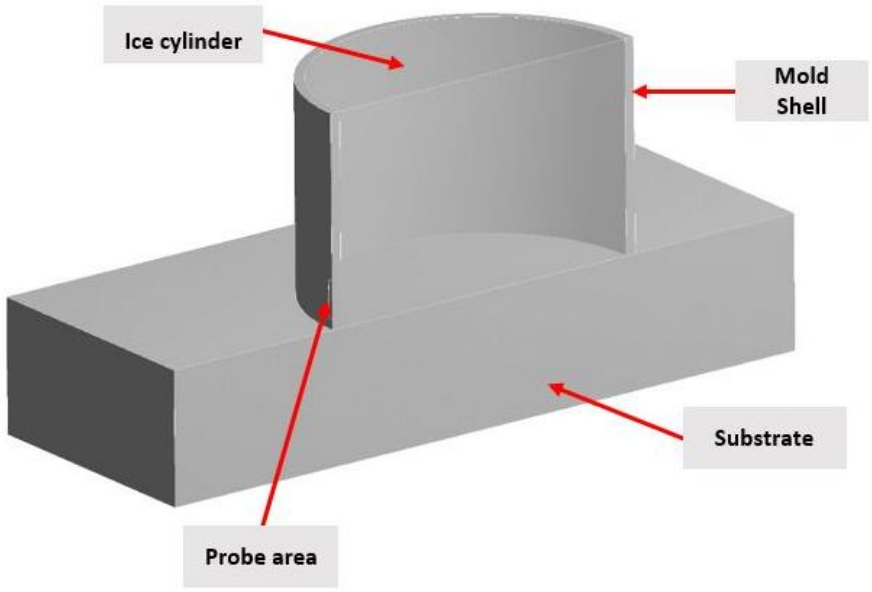

Figure 5.1. Geometric model for FE study

The geometry of the ice cylinder diameter, D, the mold shell thickness, t, the height of the displacement probe, h, and the probe contact face height, δ, are all parameters that were defined in ANSYS, thereby allowing easy rebuilding and remeshing of the model to test the importance of varying these different parameters. The probe contact area was approximated as a square region, therefore, in the half-model, is defined as δ/2 wide. In actuality, the probe will contact increasingly larger regions of the shell as the applied loading increases and the shell deforms; however, the point of this model is to capture the stresses at the ice-substrate interface rather than the stress details in the plastic mold under then probe contact face. Therefore, the fixed area approximation with dimension of 0.07inch x 0.25inch (derived from the actual cross section of probe in experiment of 0.07inch x 0.5 inch) was employed to keep the analysis linear, and avoid the substantial modelling complexity and expense associated with a nonlinear contact problem.

All three material regions were modeled as linear elastic materials with Young's Modulus Y and Poisson ratio υ. The aluminum properties are Y=68.9 GPa and υ=0.33, the ice properties are Y=9.332 GPa and υ=0.3252 [Tulk et.al, 1996], and the VeroWhite 3d-printed plastic properties are Y=2.5 GPa and υ=0.35. The boundary conditions used for the model were to approximate the clamped edges of the test plate with a fixed displacement at the model edge the displacement of the force probe was enforced over the contact patch as a prescribed nodal x-displacement at the contact patch face (Figure 5.2a), the model symmetry was enforced along the centerline of the model (Figure 5.2b)

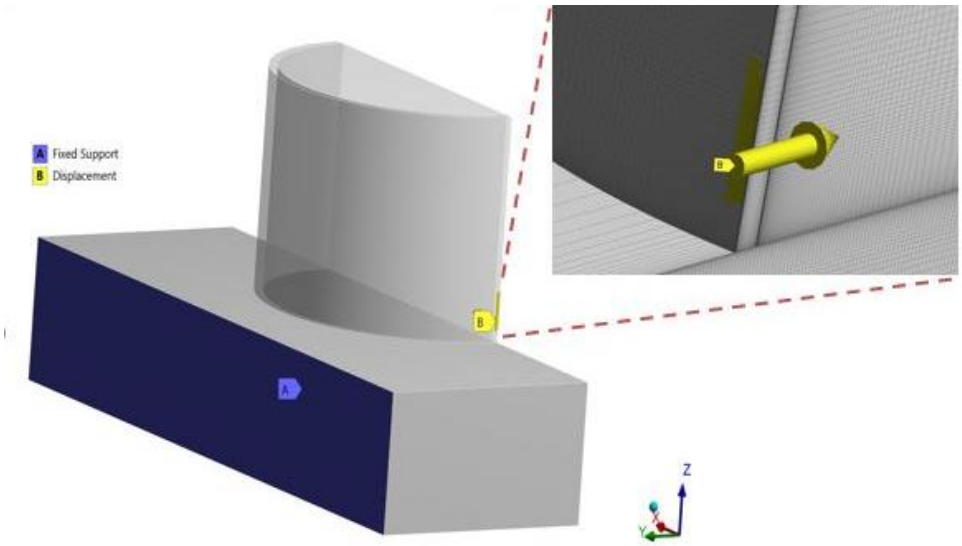

(a)

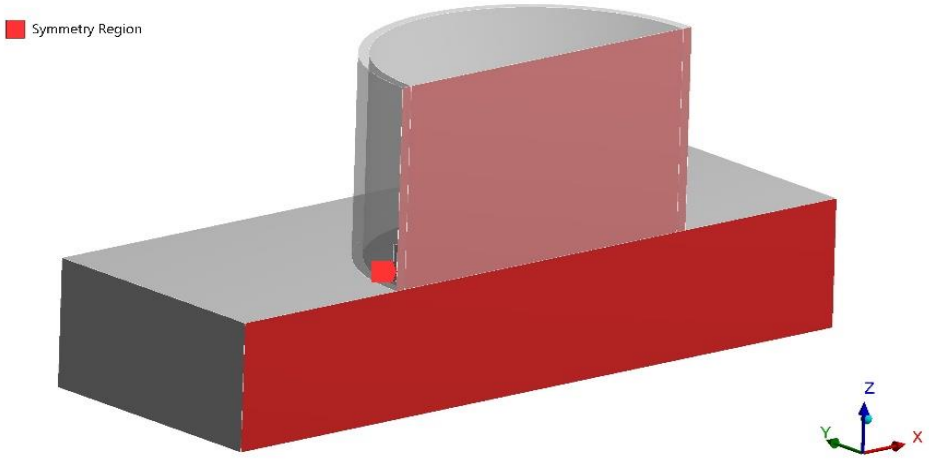

(b)

Figure 5.2. Model boundary conditions: (a) Fixed support condition (blue), close up view shows the where the probe displacement (yellow) is applied (b) Symmetry displacement (red)

The mesh was built using both the automated tetrahedral and hexahedral meshing tools in ANSYS, as well as building a structured hexahedral (sweep) mesh to control element size and shape in the vicinity of the applied load. The mesh depicted in Figure 5.3 is the finest hexahedral mesh, which employed 20 elements through the mold shell, 20 elements between the substrate and the bottom of the applied load, and 40 elements across the contact patch. The variously refined meshes were used for a mesh refinement study.

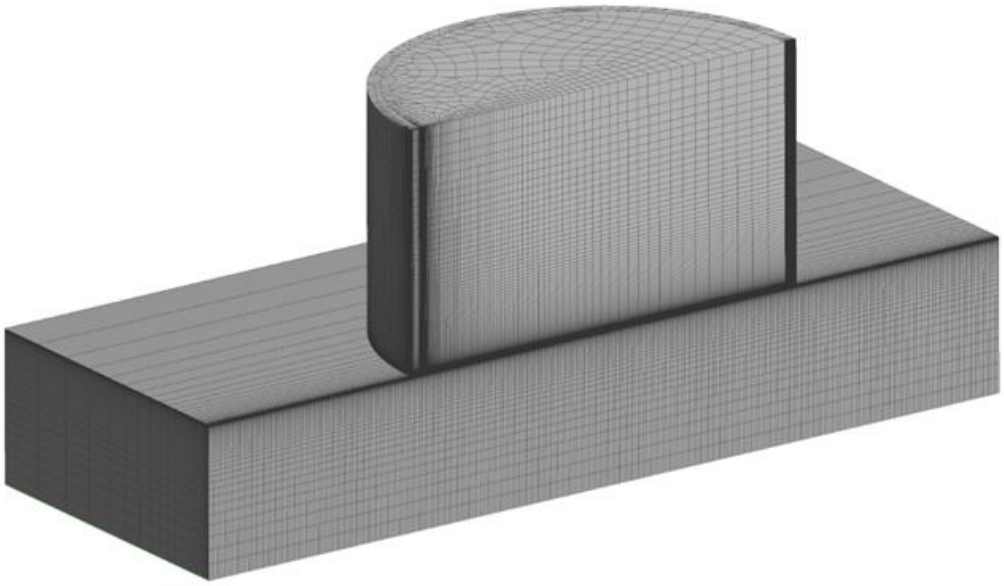

Figure 5.3 Hexahedral sweep mesh with parallel and perpendicular mesh divisions

The finite element parametric analysis was performed while considering three cases with the diameter (d), thickness (t), probe height (h) as defined in Figure 5.4 as a single variable in each case. Therefore, by letting two parameters constant, the effect of another variable could be estimated. The table (5.1) shows the input conditions for all three cases.

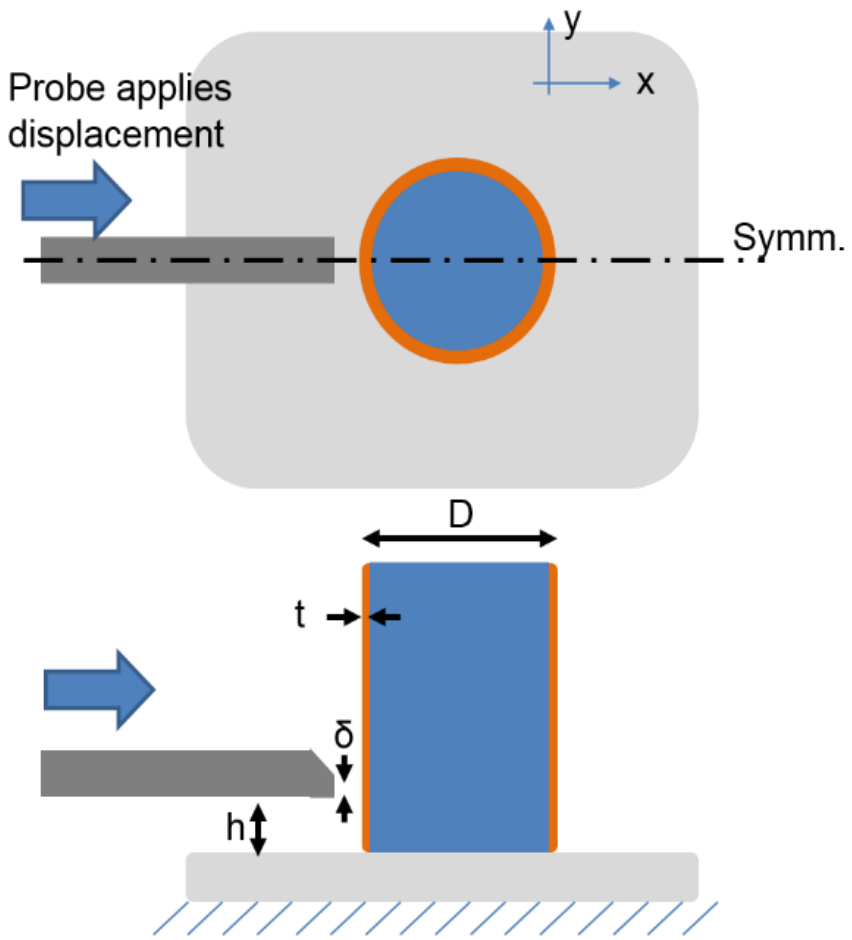

Figure 5.4 General design schematic of the ice adhesion shear test

Case	Diameter (mm)	Probe Height (mm)	Shell thickness (mm)
1	6, 8, 10, 12, 14, 16, 18, 20	0.5	0.5
2	20	0.1, 0.25, 0.5,0.75, 1, 2, 5	0.5
3	20	0.5	0.1-0.9 (+ 0.1) 1-8 (+ 1)

Table 5.1 Summary of parametric study cases

Similar to the FE study, the three cases were also investigated experimentally by using 3D printed cylinder molds of different dimensions to the range considered for finite element simulation. In order to mitigate error from water leakage, the ice columns were prepared by filling the water into molds at -8^0 C substrate plate temperature instead of ambient room temperature. An aluminum substrate was considered as a control surface for all the tests.

The mesh refinement study was performed by computing the results from a 1um probe displacement on the various meshes, using quadratic element orders. The models ranged in size from around 30,000 nodes in the very coarsest mesh, all the way up to 2 million nodes in the most refined quadratic hexahedral mesh. The total reaction force at the probe prescribed displacement face and the total force transmitted through the ice-substrate interface were computed by integrated the surface tractions over the respective surfaces. The results were computed by sampling the derived stresses at the nodes. When the mesh is sufficiently refined, it is expected that both methods should yield similar results. Additionally, the ratio of ice-substrate interface force to the reaction force at the probe was computed and plotted as a function of the mesh refinement. The mesh refinement study results are summarized by the results shown in Figure 5.5. The results in Figure 5.5 (a) and 5.5(b) show that the magnitude of the forces in the model converge when given sufficient mesh refinement. Here, the fully refined meshes with quadratic order elements were required to achieve convergence

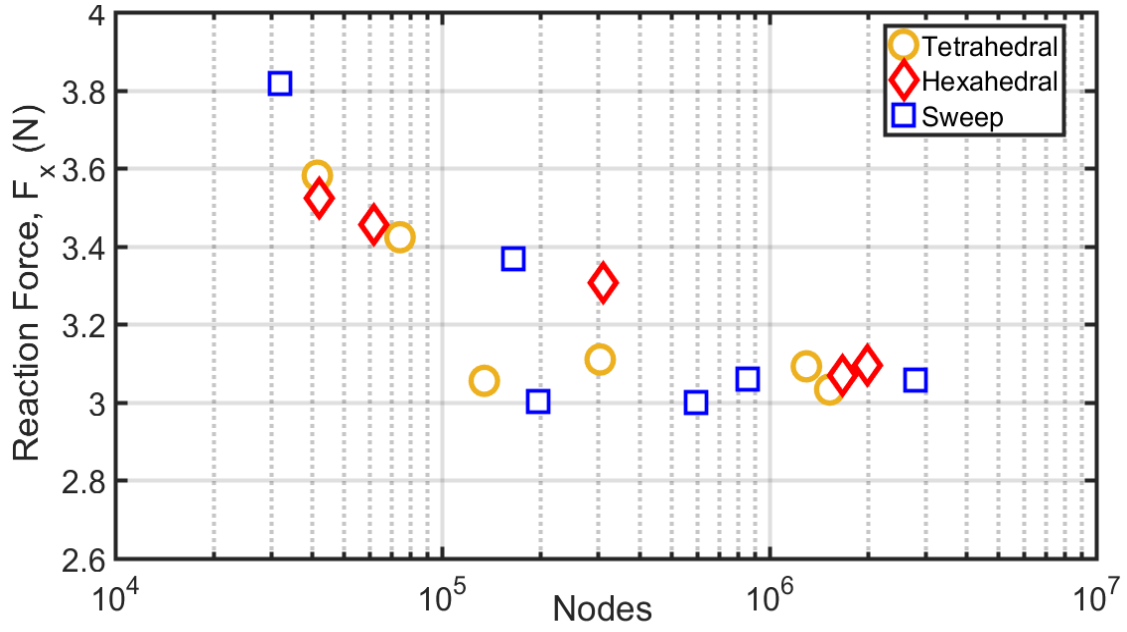

(a)

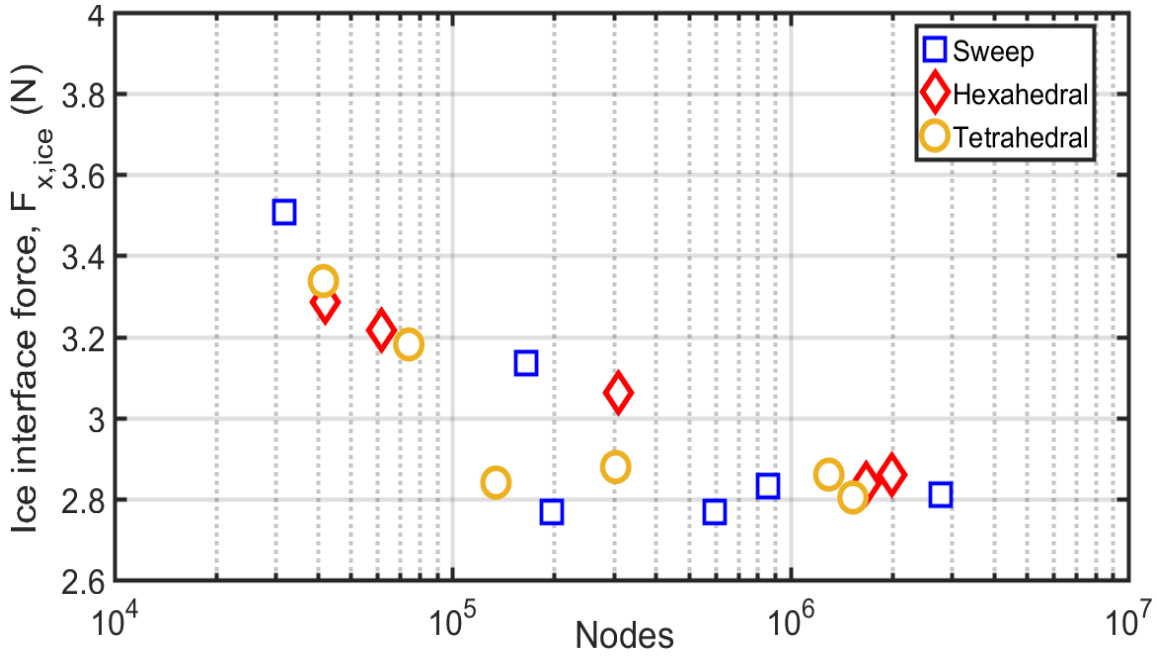

(b)

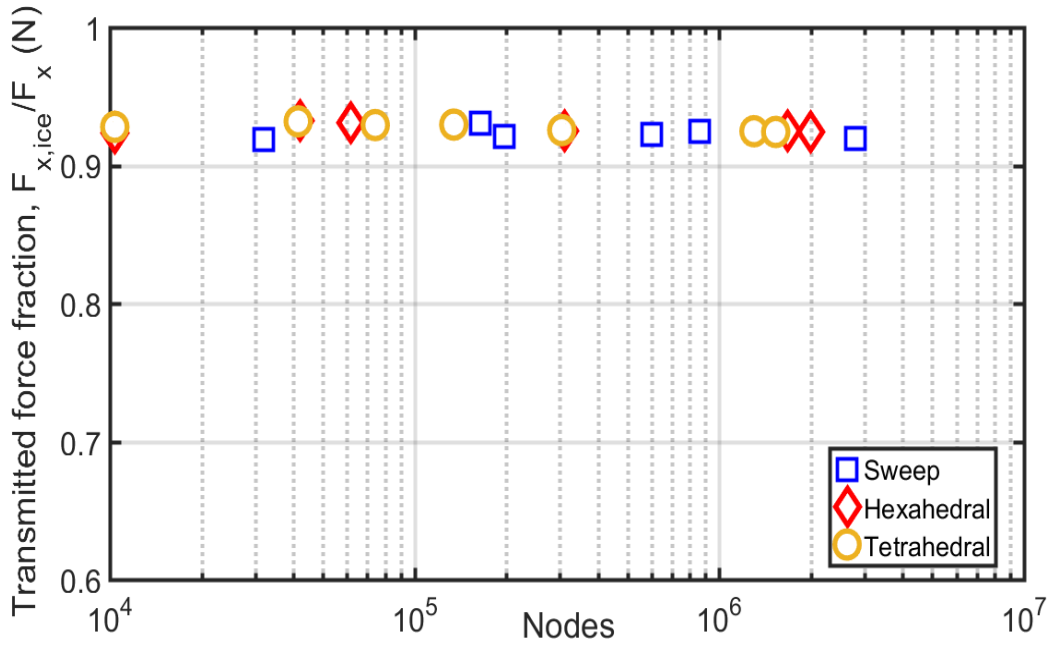

(c)

Figure 5.5. Mesh refinement study results. The results from the tetrahedral element meshes are shown in red, while the hexahedral mesh results are shown in blue. The different markers indicate different element orders and different evaluation points for the calculations. (a) Shows the probe reaction force per 1µm displacement as a function of the number of nodes in mesh model(b) Shows the force supported by the ice-substrate interface. (c) Show the ratio of the force supported at the ice-substrate interface to the applied load.

The relationship between the stress distributions and the experiment parameters such as the sample size, D, the mold shell thickness, t, and the height of the probe above the substrate, h, were investigated, to allow the comparison of the adhesion strength results.

Figure 5.6 (a) and 5.7 (a) indicates the normal stress distribution contours for 6mm and 20mm diameter ice cross section. The effect of moment is seen in both cases where there is tension (in red) on the probe side and compression on the other side (in blue). It also shows a localized downward stress near the probe contact region which could contribute to the failure initiation with bi-directional stress distribution concentrated in that region. In plane comparison for both cases shows that smaller cross section could result in prominent shear stress distribution as seen in Figure 5.6 (b) and 5.7 (b).

The effect of this stress distribution, however, can be better understood from the Figure 5.7 which compares the results for both experimental and finite element studies. The blue line shows the change in adhesion strength with different sample diameters. Based on this graph, we can identify that the adhesion stress decreases with increasing diameter where the 6mm and 20mm have values around 0.35 MPa and 0.2 MPa respectively. In addition, the finite element study shows that there is an increase of transmitted force fraction with larger dimeter or sample areas. These results could support the argument that stress distribution can influence the peak forces recorded when breaking an ice sample over the substrate. It can be explained that the smaller diameter shell requires higher adhesion stress to break the sample than the larger dimeter one because the bi-directional normal stress created due to effect of moment and probe contact (Figure 5.8 (a)) will tend to increase the stresses within the ice rather than the interface which contributes more toward cohesive failure mechanism than adhesive failure.

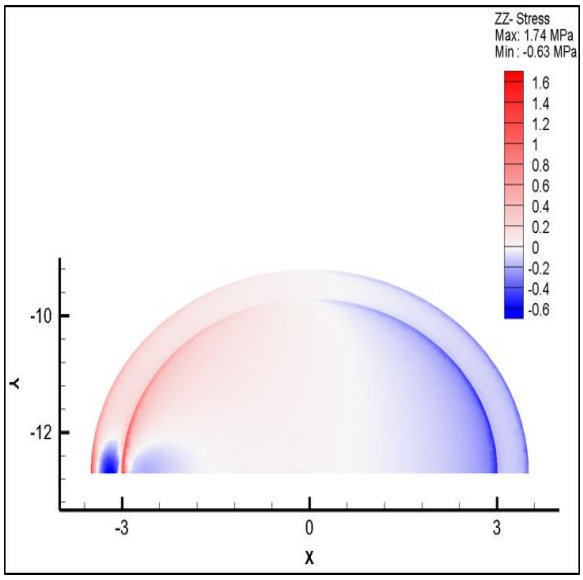

(a)

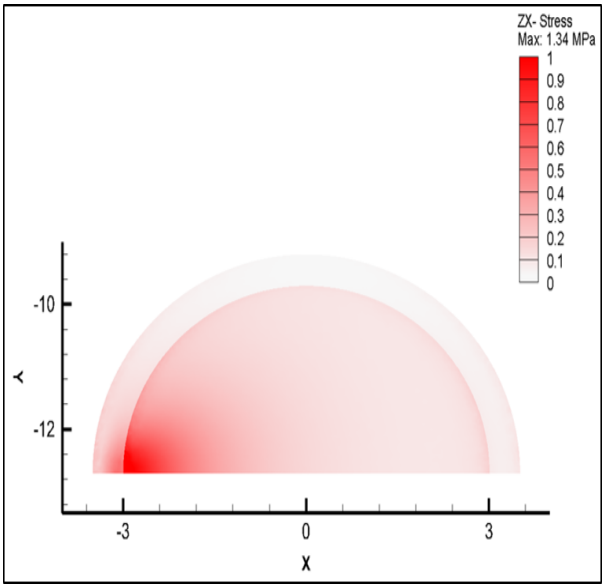

(b)

Figure 5.6. Stress distributions at the ice-substrate and mold-substrate interface for 6mm ice diameter (a) xz-shear stress distribution (b) z-stress distribution. In this plot, the probe applies the fixed displacement from the left side.

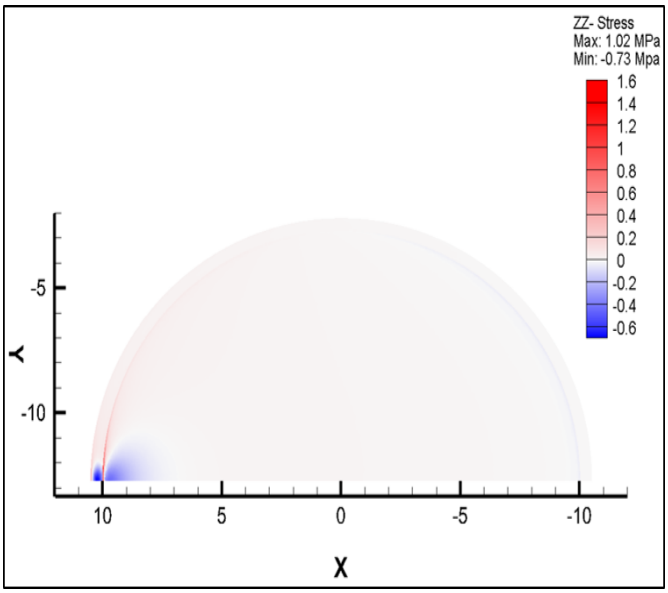

(a)

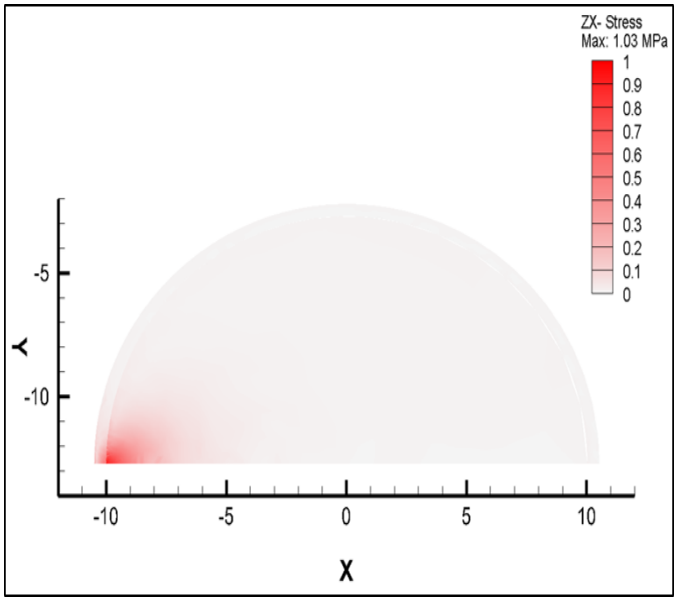

(b)

Figure 5.7. Stress distributions at the ice-substrate and mold-substrate interface for 20mm ice diameter (a) z- stress distribution (b) zx-stress distribution. In this plot, the probe applies the fixed displacement from the left side.

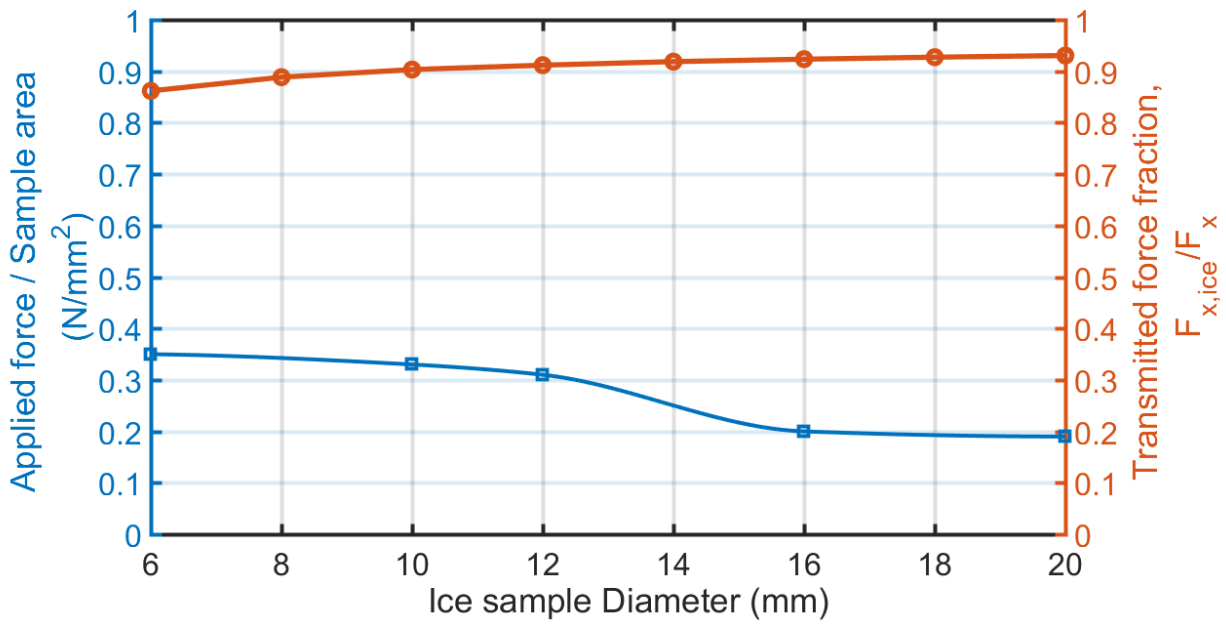

Figure 5.8. Parametric study results for diameter (a) Experimental shear strength results plotted in blue vs diameter of ice sample (b Finite element result showing force fraction vs diameter of ice sample.

The stress contours in Figure 5.9 (a) and 5.9 (b) describes normal and shear stress for probe height location of 2mm from the test surface. It is quite evident that the stress magnitudes are quite less when compared to the 0.5mm probe height case shown in Figure 5.6 (b) and 5.7 (b). The possible reason is because the probe location reduces the propagation of contact stresses to the substrate interface which result in mild stress distribution at the interface. This phenomenon can be better explained from the Figure 5.10. The finite element study shows that the transmitted force fraction steadily increases from 0 mm to 0.8 mm probe height and steadies out beyond 1 mm probe height cases. It is also interesting to see that the experimental results for adhesion strength as indicated by blue

line shows a similar effect of probe height compared to the finite element results. The adhesion strength slightly decreases from 0 to 1 mm and stays almost constant up to 5mm height. Then the line goes up for 8mm probe height case which is due to the influence cohesive failure of ice created by the moment resulted as force application moves away from the interface. This was also seen from the ice residue on the substrate after the test for 8mm probe height case. However, the overall effect of probe height on ice adhesion results is not as significant as the influence of ice sample area.

The results of the last parametric study case are shown in Figure 5.11 and figure F.12 for 5mm thick plastic shell. The stress contours in Figure 5.11 (a) and 5.11 (b) show that the increase in mold thickness reduces the stress distribution due to the slightly lower transmitted force fraction as seen in Figure 5.12. The experimental results show that a linear increase of adhesion strength with the increase of plastic shell/mold thickness. This could be due to higher force requirement for a thicker shell model when an equal displacement is applied compared to a thinner model. However, the effect of thickness can be neglected based on the results obtained here which are not significant enough to influence the overall adhesion strength and within the measurement uncertainties of the experiment.

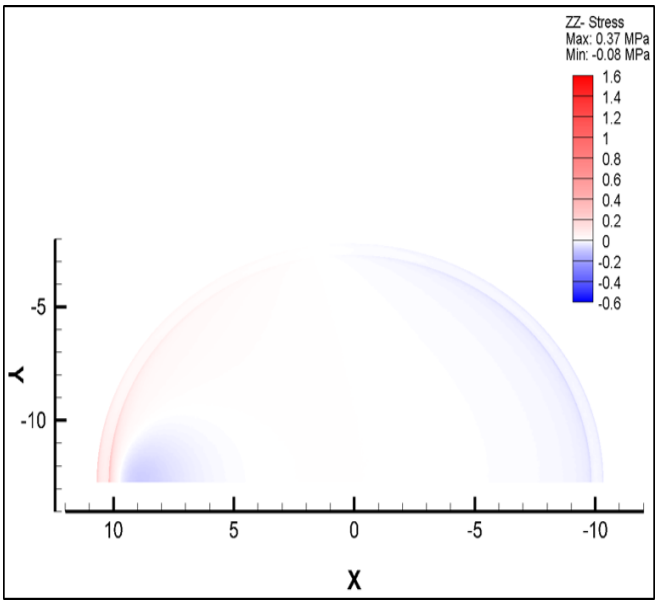

(a)

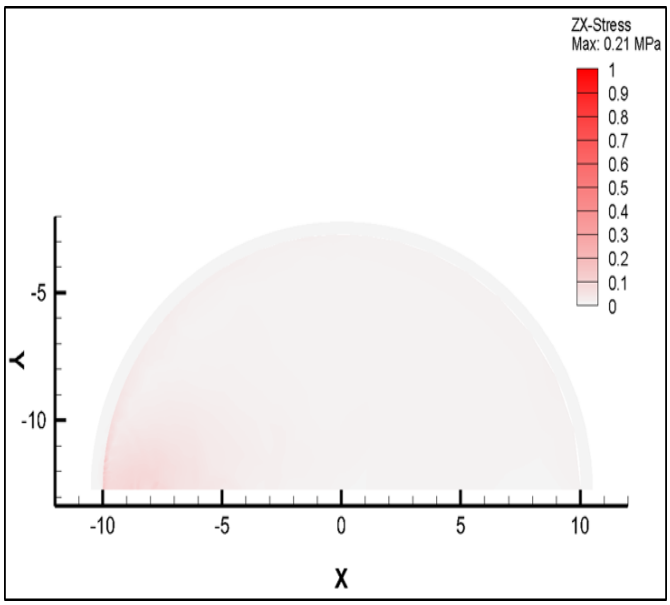

(b)

Figure 5.9. Stress distributions at the ice-substrate and mold-substrate interface for 2 mm probe height case (a) z-stress distribution (b) zx- shear stress distribution. In this plot, the probe applies the fixed displacement from the left side.

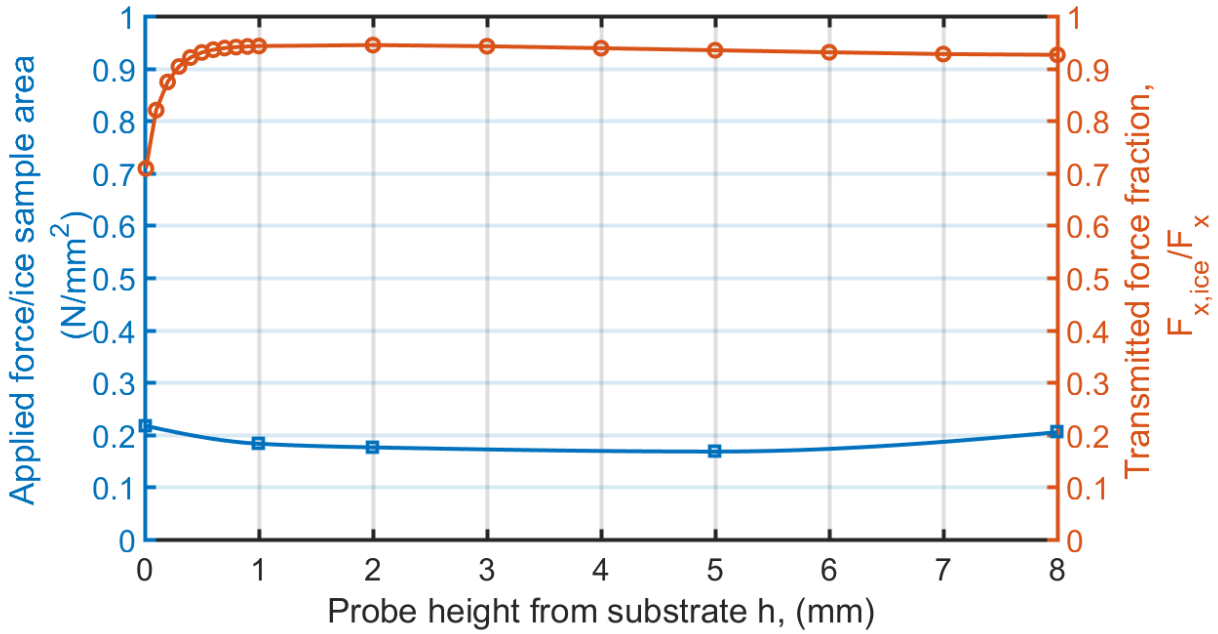

Figure 5.10. Parametric study results for probe height 'h' (a) Experimental shear strength results plotted in blue vs diameter of ice sample (b) Finite element result showing force fraction vs probe height.

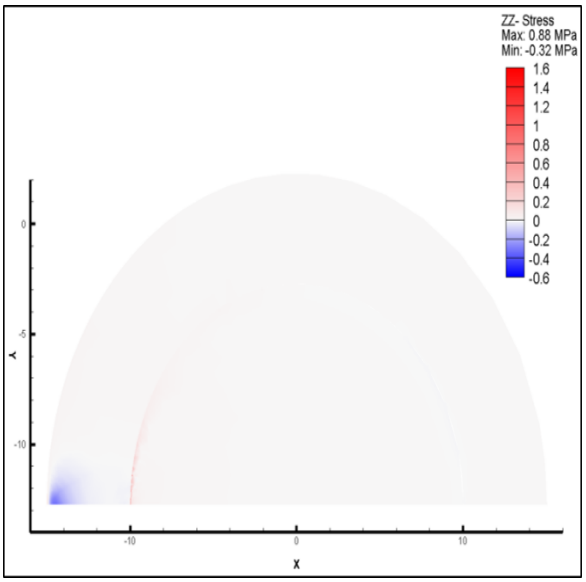

(a)

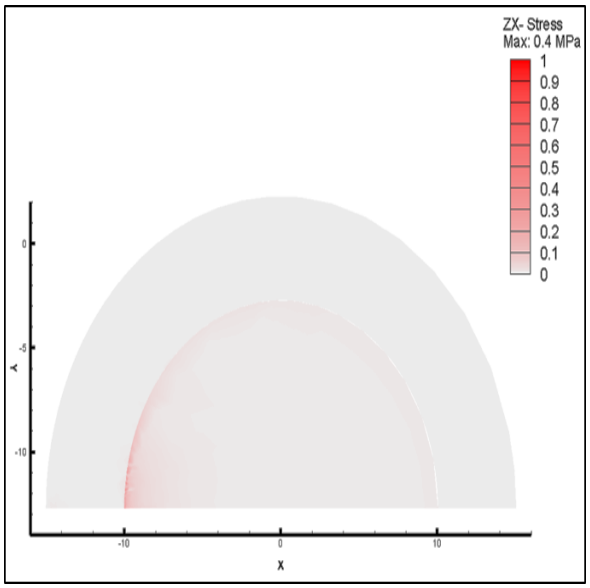

(b)

Figure 5.11. Stress distributions at the ice-substrate and mold-substrate interface for 5 mm mold thickness (a) z-stress distribution (b) zx-shear stress distribution. In this plot, the probe applies the fixed displacement from the left side.

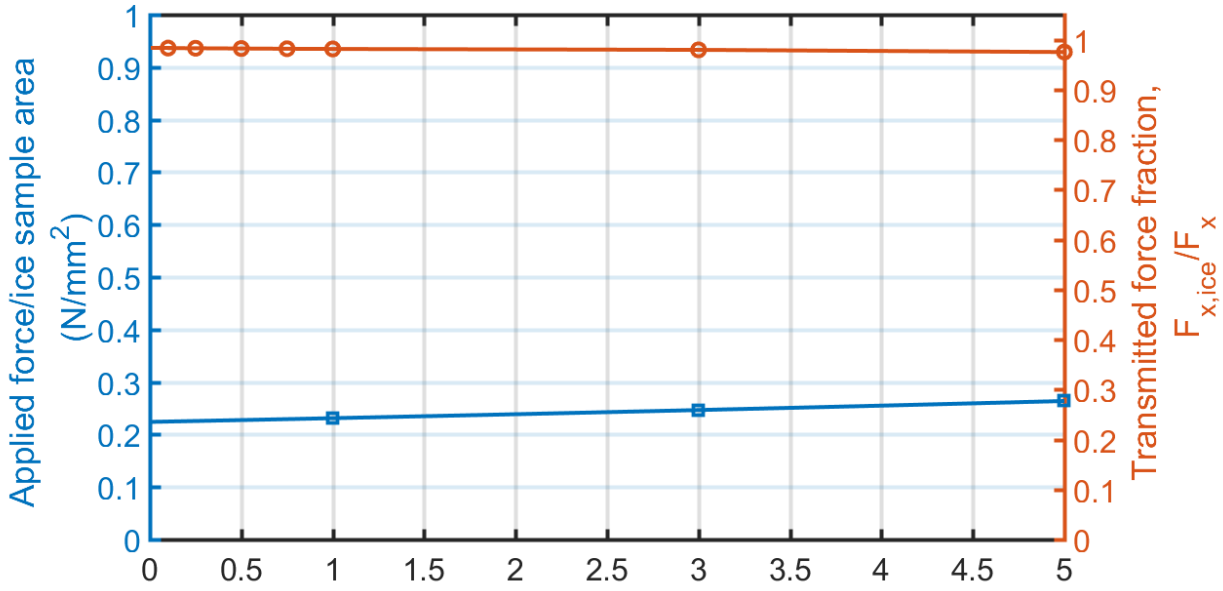

Figure 5.12. Parametric study results for thickness (a) Experimental shear strength results plotted in blue vs diameter of ice sample (b) Finite element result showing force fraction vs mold thickness.

CHAPTER 6

GENERAL CONCLUSION

The primary objective of characterizing ice adhesion over different surfaces was achieved through a new ice shear strength testing facility. Several tests were conducted on the ice adhesion test rig and adhesive shear stress was measured for 10 different materials. The ice adhesion strength revealed that SLIPS required lowest ice removal force (<0.1 MPa) among the test surfaces. However, the superhydrophobic surfaces, Hydrobead and NeverWet exhibited higher ice adhesion stress (>0.4 MPa).

To further characterize the variation in the ice adhesion strength for different materials, correlation studies were conducted. The contact angle measurements revealed the hydrophobicity and surface wettability nature of test surfaces. The comparison graphs of test surfaces revealed a linear trend in ice adhesion strength with contact angle hysteresis. Furthermore, the averaged roughness parameters were obtained from the surface topography analysis of test surfaces. The roughness and ice adhesion measurements for Neverwet and aluminum showed contrasting trends. The ice adhesion strength increased with higher roughness for hydrophilic surface and reduced for superhydrophobic surface. In addition, the ice adhesion strengths of 5 surfaces were compared at different surface temperatures -5^0 C, -10^0 C, $-15\ ^0$C, -20^0 C. It was identified that ice adhesion shear stress of hydrophilic surfaces like Aluminum and Verowhite was higher at low temperatures whereas the NeverWet and SLIPS found to have little temperature dependent variation.

Perhaps the most import feature of this study is the numerical model of the ice adhesion experiment to evaluate the stress state at the ice-substrate interface and qualitatively compare with the experimental ice adhesion measurements. The numerical parametric study showed that smaller ice sample areas could overestimate the ice adhesion results due to the presence of higher stress concentration. Moreover, the study identified an optimum distance between the force probe and the test surface for the current experimental model. In addition, variation of external shell thickness showed no significant effect on the measurement.

Based on the capability of the current method of ice adhesion measurement, it is possible to further investigate the ice phobic performance of more surfaces for anti-icing applications. In addition, the ability to obtain the force-displacement properties from this experiment can be used to develop an analytical model to characterize ice-substrate adhesion interface.

REFERENCES

Appiah-Kubi P (2011) US Inflight Icing Accidents and Incidents, 2006 to 2010. University of Tennessee

Bassey CE, Simpson GR (2007) Aircraft ice detection using time domain reflectometry with coplanar sensors. In: IEEE Aerospace Conference Proceedings. IEEE, pp 1–6

Boluk Y, 1996 Adhesion of freezing precipitates to aircraft surfaces, Transports Canada Publication No TP 12860E Quebec, Canada

Bragg, M. B., Broeren, A. P., and Blumenthal, L. A., Iced-airfoil aerodynamics, Progress in Aerospace Sciences, vol. 41, Jul. 2005, pp. 323–362.

Cao, L., Jones, A. K., Sikka, V. K., Wu, J., and Gao, D., Anti-icing superhydrophobic coatings., Langmuir: the ACS journal of surfaces and colloids, vol. 25, Nov. 2009, pp.1244-8.

Ensikat HJ, Ditsche-Kuru P, Neinhuis C, Barthlott W. Superhydrophobicity in perfection: the outstanding properties of the lotus leaf. Barthlott W, Koch K, eds. Beilstein Journal of Nanotechnology. 2011; 2:152-161. doi:10.3762/bjnano.2.19.

Epstein, A. K., Wong, T.-S., Belisle, R. a, Boggs, E. M., and Aizenberg, J., "Liquid-infused structured surfaces with exceptional anti-biofouling performance.," Proceedings of the National Academy of Sciences of the United States of America, vol. 109, Aug. 2012, pp. 13182–7.

FAA advisory circular AC 91-74B- Pilot Guide: Flight in icing conditions, 2015, https://www.faa.gov/regulations_policies/advisory_circulars/index.cfm/go/document.information/documentID/1028388.

Ghalmi, Z., Menini, R., Farzaneh, M., Theoretical studies and quantification of ice adhesion mechanisms, Proceeding of the 13th International Workshop on Atmospheric Icing of Structures, IWAIS Andermatt (2009)

Green SD (2006) A study of US inflight icing accidents and incidents, 1978 to 2002. In: 44th AIAA Aerospace Sciences Meeting and Exhibit, Reno, Nevada.

Hansman RJ, Kirby MS (1987) Comparison of wet and dry growth in artificial and flight icing conditions. J Thermophys Heat Transf 1:215–221

Hassan, MF & Lee, Hp & P Lim, S. (2010). The variation of ice adhesion strength with substrate surface roughness. Measurement Science and Technology. 21. 075701. 10.1088/0957-0233/21/7/075701.

Heydari, G, Toward Anti-icing and De-icing Surfaces: Effects of Surface Topography and Temperature, Doctoral Thesis, KTH Royal Institute of Technology, 2016.

Kasaai, MR and Farzaneh, M., Evaluation of mechanisms of ice adhesion on power network equipment. Proceedings of OMEGA, 23 International Conferences of Offshore Mechanics and Arctic Engineering, Vancouver, British Columbia, Canada, June 2004.

Jellinek, H.H.G., Ice adhesion, Canadian Journal of physics. Vol (40), 1962.

Lee, L.H., Fundamentals of Adhesion, Plenum Press: New York, 1991.

Liu.Y, LK Li, Z. Ning, W. Tian and H. Hu, “Experimental Investigation on the Dynamic Icing Process over a Rotating UAS Propeller", AIAA Journal of Power and Propulsion, 2017.

Maitra, T., Tiwari, M. K., Antonini, C., Schoch, P., Jung, S., Eberle, P., and Poulikakos, D., On the nanoengineering of superhydrophobic and impalement resistant surface textures below the freezing temperature, Nano Letters, vol. 14, 2014, pp. 172–182.

Makkonen, Lasse. (2012). Ice Adhesion —Theory, Measurements and Countermeasures. Journal of Adhesion Science and Technology – Journal of Adhesion science technology. 26. 413-445. 10.1163/016942411X574583.

Meuler J, Adam & David Smith, Jonathan & K Varanasi, Kripa & Mabry, Joseph & Mckinley, Gareth & E Cohen, Robert. (2010). Relationships between Water Wettability and Ice Adhesion. ACS applied materials & interfaces. 2. 3100-10. 10.1021/am1006035.

Petrenko, V.F. and Ryzhkin, I.A., Surface states of charge carries and electrical properties of the surface layer of ice, J. phys. Chem. B, Vol (101), pp 6285-6289, 1997.

Petrenko, V.F. & Whitworth, R.W., Physics of ice, New York, 1999.

Sayward, JM., Seeking low ice adhesion, 1979, U.S. Army Cold Regions Research and Engineering Laboratory.

Schulz, M. and Sinapius, M., Evaluation of Different Ice Adhesion Tests for Mechanical Deicing Systems, SAE Technical Paper 2015-01-2135, 2015, doi:10.4271/2015-01-2135.

Tulk, C. a., Gagnon, R. E., Kiefte, H., and Clouter, M. J., Elastic constants of ice VI by Brillouin spectroscopy, The Journal of Chemical Physics, vol. 104, 1996, p. 7854.

Vorobyev, A. Y., and Guo, C., Multifunctional surfaces produced by femtosecond laser pulses, Journal of Applied Physics, vol. 117, Jan. 2015, p. 033103.

Waldman, RM and Hu, H., High-Speed Imaging to Quantify Transient Ice Accretion Process over an Airfoil, Journal of Aircraft, Vol. 53, No. 2 (2016), pp. 369-377.

Wilen, LA, J.S. Wettaufer, M. Elbaum, M. Schick, Dispersion-forces effects in interfacial premeltingof ice, Physical Review B, Vol (52), pp 12426-12433, 1995.

Zhu, L., Xue, J., Wang, Y., Chen, Q., Ding, J., and Wang, Q., Ice-phobic coatings based on silicon-oil-infused polydimethylsiloxane., ACS applied materials & interfaces, vol. 5, 2013, pp. 4053–62.

APPENDIX

TESTING OF DURABLE ICEPHOBIC COMPOSITE COATING FOR AIRCRAFT ICING MITIGATION

Rye Waldman, Linkai Li, Prashanth Beeram and Hui Hu
Department of Aerospace Engineering, Iowa State University
9 September 2016

Five commercial proprietary coatings denoted “A1”, “A2”, “A4”, “A5”, and “A6”, were tested at Iowa State University Department of Aerospace Engineering to gauge the coatings’ ice adhesion performance. The coatings were subjected to two tests: 1) the coatings were applied to symmetric airfoil models and tested under a glaze ice inflight impact ice condition in the ISU Icing Research Tunnel facility, and 2) the coatings were applied to small aluminum test plates and tested in a shear force adhesion strength facility.

The test model used in the present study is a rapid prototyped symmetric NACA0012 airfoil model with a chord length of 152.4 mm. The test airfoil model spans the test section, therefore, pseudo 2D flow is assumed. The coatings were tested on symmetric airfoil models mounted in the ISU-UTAS-IRT facility and tested at a representative glaze ice condition. The test condition was a 40 m/s wind speed (V_∞), -8°C air temperature (T), and 2.0 g/m^3 liquid water content (LWC). The wing was tested at 5° angle of attack. To record the ice accretion process on both the suction and pressure sides of the wing, each coated wing was tested twice, once at +5° angle of attack to observe the suction side, and once at -5° angle of attack to observe the pressure side. The 720x660

pixel^2 images were recorded at 10 frames per second for 10 minutes to provide a time sequence of the ice growth and shedding during the test. After each test, the iced airfoil was photographed.

In the following figures (Coating-A2 as an example), the broken red line denotes the boundary between the test surface on the left and the control surface on the right. The camera is oriented with the airflow from the top of the image toward the bottom. For each of the tests where ice shedding was observed, an image pair is shown highlighting an ice shed event.

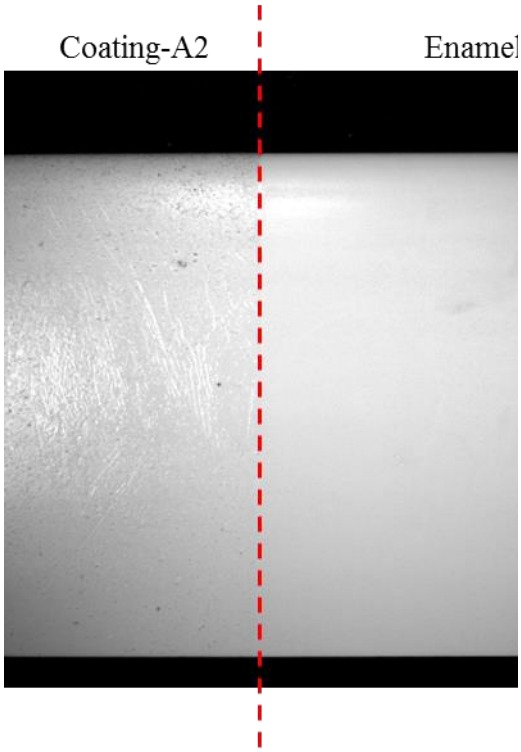

a. T=0 s

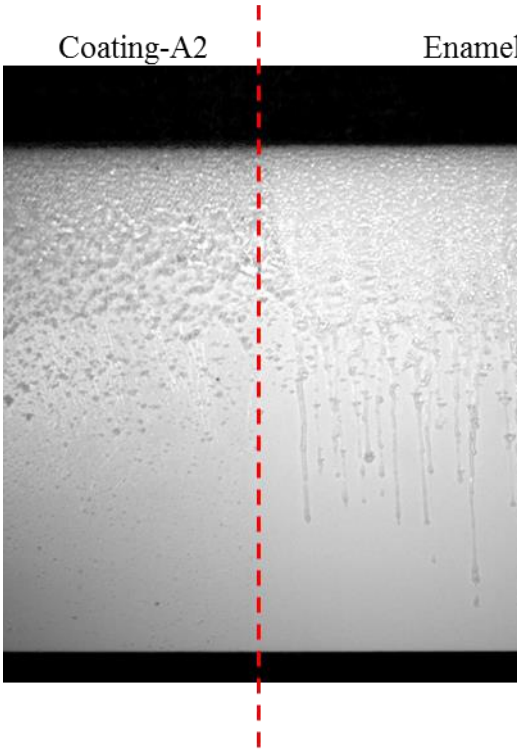

b. T=60 s

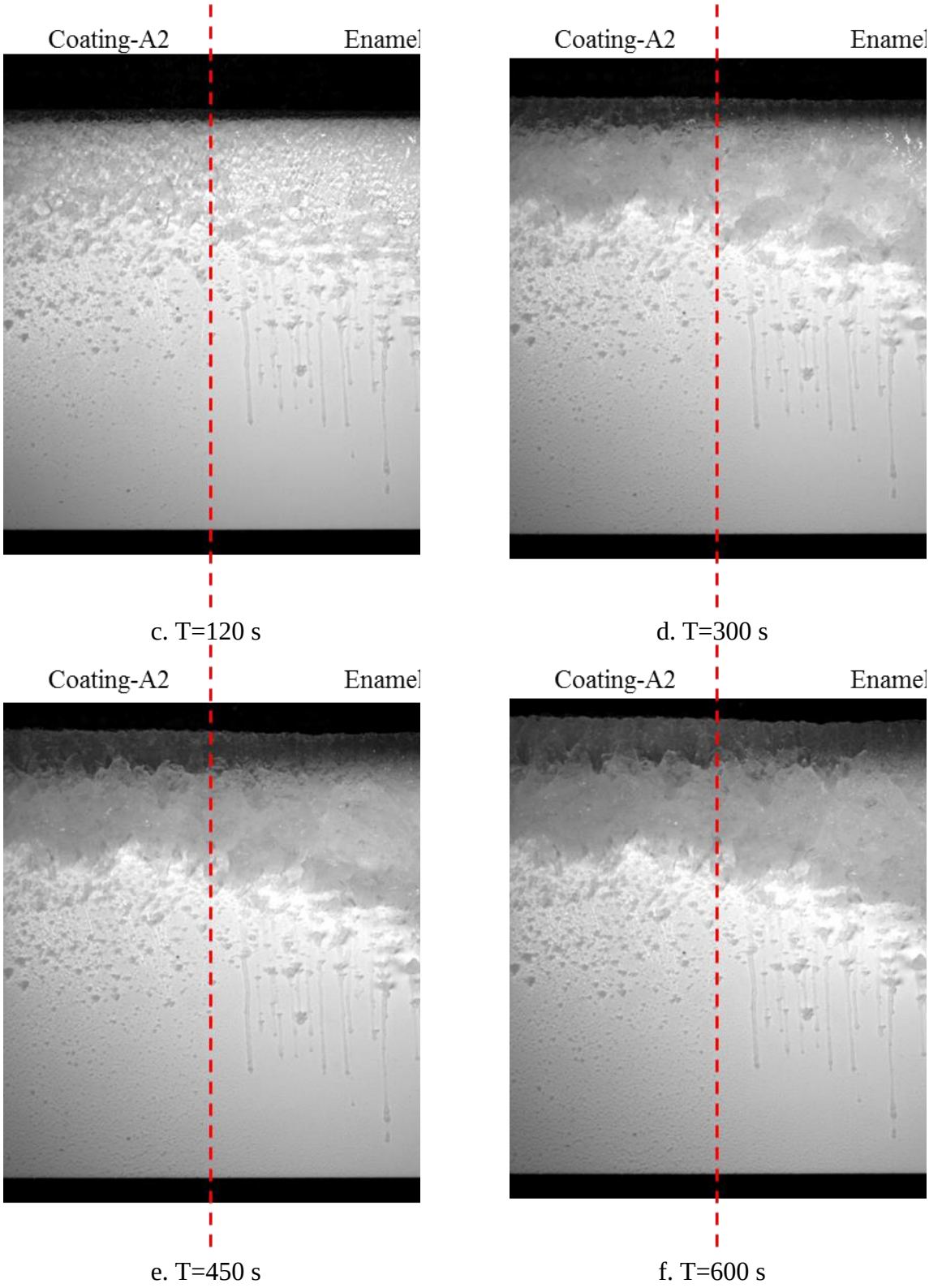

c. T=120 s

d. T=300 s

e. T=450 s

f. T=600 s

Time sequence of ice accretion process (Pressure Surface)
(Coating-2, V_∞=40 m/s, LWC=2 g/m^3, T=-8℃, α=-5 °)

Final ice accretion shape on the model (Pressure surface)
(Coating-A2, V_∞=40 m/s, LWC=2 g/m^3, T=-8℃, α=-5 °)

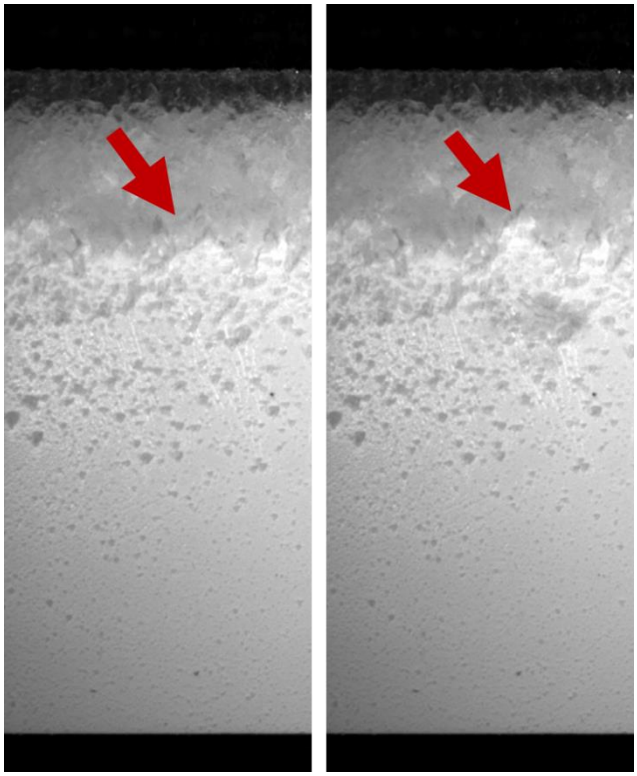

Ice shedding images pair (Frame 2550 & 2551)
(Coating-A2, V_∞=40 m/s, LWC=2 g/m^3, T=-8℃, α=-5 °)

The test coatings A1–A6 all show reduced adhesion strengths; however, the amount of adhesion strength reduction varies across the different coatings. To compare the relative adhesion reduction performance of the coatings, the Adhesion Strength Reduction was calculated by dividing the control's adhesion strength by each coatings adhesion strength. The worst performing coating is A1, which only reduced adhesion strength by a factor of 3 compared to the Rustoleum enamel. The best performing coatings were A6, A2, and A4, each of which reduced the adhesion by a factor of more than 10.

The wind tunnel tests and adhesion strength tests indicate that the coatings A2, A4, A5, and A6 demonstrate observable reductions in the adhesion strength of ice. The 3 coatings with highest Adhesion Strength Reduction were also the same coatings that produced the most ice shedding events in the wind tunnel tests. A1 was the poorest performing coating, both in terms of producing the smallest Adhesion Strength Reduction of 3.13, and in terms of having no ice shedding in the wind tunnel test.

The wind tunnel tests indicate that the reduced adhesion strength allows the aerodynamic stresses to remove some of the ice features on the wing; however, the ice shedding is restricted to the pressure side of the airfoil where the flow is attached and the ice formations are individual ice feathers, which attach at a small area and protrude into the airflow. At the leading edge, the water deposited on the wing forms a thin liquid film that coats a larger surface area and remains low inside the boundary layer where the local air speeds are small. The aerodynamic forces near the stagnation point vanish, and allow a sheet of ice to form wrapped around the leading edge. Here, the bond of the ice to the surface is much greater than the aerodynamic forces, and the ice remains attached,

anchored to the surface and pressed onto the leading edge by the stagnation pressure. As the ice at the leading edge grows, the flow over the suction side of the wing separates, therefore there is insufficient high-speed air flowing over the ice feathers behind the leading edge ice to produce any shedding.

In comparison to the control surface, which was finished to a very smooth polish, the test surfaces A1–A6 all exhibit substantial surface roughness. The rough surfaces protrude out into the boundary layer, and are localized water collection points. The ice accretion on the enamel surface is initially dominated by a water film that runs back over the smooth surface, eventually breaking into rivulets that continue along the surface. The ice feathers on the enamel surface originate only at the beads along the rivulets, or from the local peaks the water film instability. The rough surface of the A1–A6 coatings collect water further along the airfoil simply because they stick out into the flow. By smoothing the coatings much of the ice collected beyond the trailing edge could be avoided.

Differences in the hydrophobicity of the coatings to the enamel coating results in thicker ice growth at the leading edge compared to the enamel control. All of the A1-A6 coatings exhibit hydrophobic behavior (contact angle > 90°) while the enamel coating is slightly hydrophilic (contact angle < 90°). This results in the water beading up on the test coatings, which protrude into the flow freezing faster and initially causing increased leading edge roughness. Subsequent water that impinges at the leading edge gets caught in the roughness, and freezes closer to the leading edge. The enamel surface allows the water to wet the wing and run back, transporting more water downstream. Therefore, the ice covers more of the wing, but has a smaller profile on the enamel coating, while the leading edge ice accretion remains smaller in profile.